Chapter 6
Ultrafast Laser Micro and Nano Processing of Transparent Materials—From Fundamentals to Applications

Manoj Kumar Bhuyan and Koji Sugioka

Abstract The distinctive features of ultrafast lasers, such as the extremely high peak intensity associated with their ultrashort pulse duration, enable the machining of materials whose band gaps are larger than the photon energies of the laser due to the nonlinear nature of photon absorption by matter. As a result, processing of transparent materials at micro and nanoscale levels can be achieved using ultrafast lasers, which is a matter of particular relevance in the fields of electronics, healthcare, photonics, and energy harvesting. By using ultrafast laser beams that possess a standard Gaussian spatial profile, and by exploiting nonlinear light-matter interaction confinement schemes, fabrication resolutions have declined to just a few tens of nanometers on the surface, and a few hundreds of nanometers inside most transparent materials. However, it is difficult to maintain such fabrication resolutions, especially at nanoscale levels, when forming high aspect ratio (length over diameter) structures inside transparent materials. This issue can be addressed using novel focusing strategies and spatiotemporal beam shaping techniques. In this chapter, we will begin by reviewing the basic concepts of, and experimental methodologies related to, laser machining techniques. Then, machining strategies that have been adopted to facilitate high fabrication resolutions and long fabrication lengths using standard Gaussian laser beams are discussed, along with other competent techniques, thereby highlighting the underlying fundamental mechanisms and their applicability for material processing such as for drilling and cutting. Furthermore, the impact of spatiotemporal beam shaping on material processing is discussed, with a special focus on applications of non-diffractive optical beams for fast and flexible material processing. Finally, we provide a futuristic viewpoint on the potential for achieving super-resolution, yet high-aspect-ratio, material fabrication.

M. K. Bhuyan · K. Sugioka (✉)
RIKEN Center for Advanced Photonics, RIKEN, Wako, Saitama 351-0198, Japan
e-mail: ksugioka@riken.jp

M. K. Bhuyan
e-mail: manoj.femto@gmail.com

6.1   Introduction

Ultrafast lasers, defined as lasers with pulse durations shorter than a few picoseconds (ps), are excellent tools for transparent material processing. The ability of such lasers to generate a high peak intensity squeezed into an ultrashort time window makes it possible for them to trigger nonlinear photon absorption processes (described in detail in the following section), leading to optical breakdown of ideally any material which is the basis of ultrafast laser machining technique [1–4]. Furthermore, as will be discussed below, when a laser pulse is focused with an adequate amount of energy, nonlinear photon absorption can occur not only on the surface of most transparent materials, but also inside them, at a very confined region near the focal volume. This absorbed photon energy can induce a range of photo-chemical and photo-physical processes such as cross-linking (polymerization), bond breaking (refractive index alteration), and ablation (material removal in gas, liquid and solid phase), over timescales ranging from femtoseconds to milliseconds. Likewise, material processing down to the nanoscale, and (most importantly) in three-dimensional (3D) space, can be realized using lasers, which has a great deal of relevance in multiple fields including electronics, photonics, healthcare, and energy harvesting. Since there have been numerous research efforts made to accelerate the field of laser-assisted material processing in recent years, this chapter discusses some of the more important approaches, while concentrating primarily on the processing of transparent materials.

   As mentioned above, the basic advantages of laser machining techniques lie with their ability to produce localized material breakdown via optical means, thereby causing modifications to material's physical properties. From a fundamental viewpoint, there are three generic aspects associated with ultrafast laser induced optical breakdown of matter.

(i) *The near-instantaneous transfer of energy from a laser pulse to the electronic (sometimes referred to as electron-hole plasma) sub-systems of the material* via *non-linear ionization mechanisms*. Depending on the laser intensity level, the nature of ionization mechanisms can be multi-photon (several photons becoming absorbed simultaneously, thus promoting electrons from the valence to the conduction band of the material), single-photon (conduction band electrons becoming energized by directly absorbing single photons) and scattering (conduction band electrons with energy levels exceeding the material bandgap that can knock additional electrons from the valence band, thereby resulting in an avalanche process). Although, the individual contributions of each ionization mechanism are difficult to calculate (and are still a subject of debate), multi-photon ionization is assumed to play an important role in cases involving dielectric materials possessing wide band gaps, with (ideally) no available free electrons. Note that metals have vast amounts of free electrons and can be energized on a single-photon basis. Additionally, narrow bandgap materials, such as semiconductors, can undergo single photon absorption.

(ii) *Energy transfer from electronic sub-systems to the lattice* via *electron-phonon scattering processes occurring on femtosecond to picosecond timescales*,

(iii) *Lattice re-organization and stabilization on timescales ranging from femtoseconds to microseconds*. Quantitatively, in the case of dielectrics, when the laser intensity exceeds the 10^{12} W/cm^2 level, a laser induced free electron density can be achieved in the range of 10^{18}/cm^3 to the critical density (i.e., nearly 10^{21}/cm^3), which has a strong potential to trigger lattice re-organization during the relaxation cycle of excited matter. The material relaxation can take several pathways [5–8], and can result in various types of material modifications [5, 9–11]. For example, the manifestation can be in the form of a surface crater via ablation, an increased refractive index structure via molecular rearrangement, or a decreased refractive index structure, such as a void formed via localized explosion and stress relaxation inside most transparent materials. More scenarios that consider the experimental findings related to laser structuring are discussed in later sections. In brief, the resultant material modifications depend primarily on the laser assisted energy deposition dynamics. Specifically, the amount of (and the rate at which) optical energy is deposited into or onto the material.

From an experimental viewpoint, the energy deposition dynamics for a given material are controlled via laser beam parameters such as the beam profile, pulse energy and temporal duration, wavelength, polarization state, and focusing geometry. For example, ultrashort laser pulses (those in the femtosecond (fs) to picosecond range) that suppress thermal effects during ablation process, are useful for high-quality material fabrication. In contrast, nanosecond laser pulses are suitable for material processing based on melting and annealing. Laser wavelength is also critical for the machining of biological materials. From an application viewpoint, single-laser-pulse based material processing provides the best option in terms of throughput and fabrication quality. However, since multiple laser pulses can also be employed, especially when the single pulse energy is insufficient to trigger a material phase change, this methodology can provide high-speed and economical material processing using currently available very high repetition rate (up to few hundred MHz) ultrafast lasers with nanojoule energy levels. In multiple-pulse-exposure cases involving pulse energies of just a few microjoules, the resultant material modifications are strongly dependent on the laser polarization state. A spatially homogeneous laser beam profile (which otherwise has a Gaussian profile in the radial direction), such as a flat-topped profile, is also required for uniform energy deposition, especially for large area material processing applications such as sintering, lithography, and pulsed laser deposition [12].

6.2 Direct Fabrication Using Gaussian Laser Beams

This section first introduces Gaussian laser beam-based material processing techniques aimed at the direct fabrication of micro and nanostructures, and then high-

lights their underlying mechanisms and technical capabilities. Along with surface and bulk processing facilitated by localized (point-like) energy deposition, elongated structuring facilitated by aberration effects and nonlinear beam propagation dynamics are also discussed. Nanoscale structuring techniques based on near-field optical phenomena are then considered, after which a non-laser based (ion beam) machining technique is reviewed to provide a useful comparison.

6.2.1 Standard Fabrication Approach

The methodology of standard laser machining techniques involves focusing a laser beam through a lens (often a microscope objective lens) onto or into a material in order to produce a local change in the physical properties of the treated material. An altered material feature (such as a crater or index change) is mostly referred to as a "structure" throughout this chapter. Figure 6.1a shows a schematic diagram of a *laser based surface structuring technique*. Although the beam (ideal Gaussian profile and wavelength λ) spot size (diameter) S_G at the focal point of an objective lens with a numerical aperture (NA) is $S_G = 1.22 \, \lambda/(2 \, \text{NA})$, the lateral dimension of the machined structure often becomes smaller than the beam spot size due to the threshold effect over the spatial distribution of the laser intensity. Additionally, various researchers [13–15] have reported that machined structure sizes can be reduced to a few tens of nanometers (which is much smaller than the irradiation wavelength and diffraction spot size), clearly indicating non-linear energy deposition into the material. For instance, Joglekar et al. [13] demonstrated nanoscale structuring of Corning 0211 glass using 600 fs laser pulses at wavelengths of both 527 and 1053 nm, which were focused using an objective lens with an NA of 1.3. Figure 6.1b shows scanning electron microscopy (SEM) images of nanostructures (size down to 30 nm) machined on glass using a single 7.5 nJ energy laser pulse at a 527 nm wavelength. The lateral size of the machined structure was also observed to be in the range from a few tens of nanometers to a micron, as shown in Fig. 6.1c, where 1053 nm wavelength laser pulses are employed. Here, the sub-wavelength scale structuring is attributed to the nonlinear energy confinement mechanisms that lead to ablation events. Note that ablation is a threshold-defined process. This implies that only the material region within which the laser intensity exceeds the threshold value, i.e., 10^{12}–10^{13} W/cm^2, gets ablated. Hence, the lateral size of the ablated zone that defines the surface machining or fabrication resolution can be smaller than the diffraction limit. The deterministic nature of the above-mentioned nanoscale structuring raised concerns over widely accepted nonlinear ionization mechanisms such as multiphoton, tunneling, and avalanche ionization. Joglekar et al. [14] argued for a novel ionization mechanism. Specifically, that Zener ionization could play a role at near-ablation threshold intensity regime.

Although single-pulse structuring techniques involving ultrashort Gaussian beams have been very successful in producing high-quality nanoscale structures (i.e., with almost no heat affected zone around the structure), the techniques suffer from poor machining throughput. Additionally, scaling of structure dimensions (mainly lat-
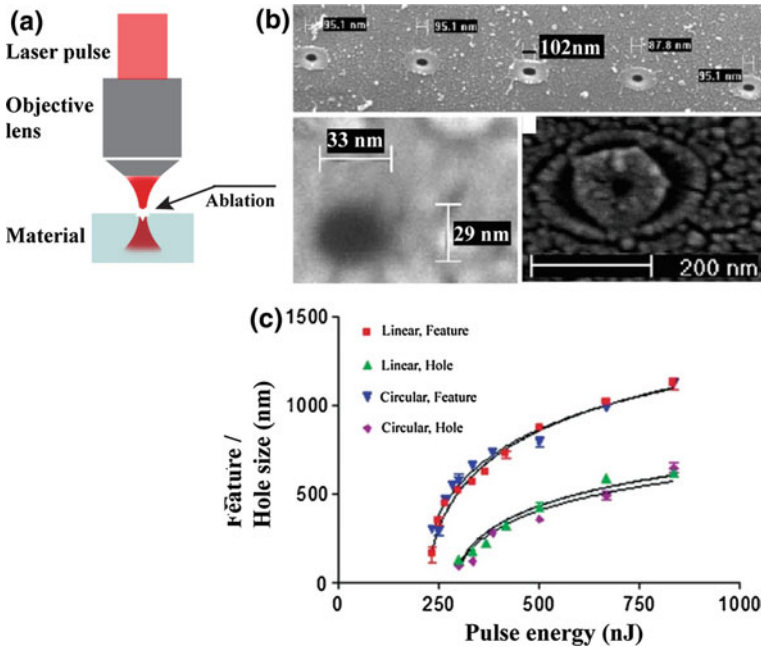
Fig. 6.1 Laser-based surface structuring technique: **a** Typical machining scheme showing a laser pulse focused onto a material through an objective lens. **b** SEM images of single laser pulse (600 fs pulse duration, 527 nm wavelength, energy 7.5 nJ) induced structures on Corning 0211 glass surface. **c** Variation of structure size as a function of laser energy in case of single pulse (600 fs pulse duration, 1053 nm wavelength) excitation of glass [13]. Reproduced with permission from the American Institute of Physics (AIP)

eral) is another issue in such machining schemes. A number of early experiments exploited multiple pulse structuring in order to address the above-mentioned issues. For example, multiple laser pulses (typically less than 10^3) at a repetition rate in the kHz range were used to produce large structures on metals, semiconductors, and dielectrics by invoking incubation effects [16, 17] assisted by laser induced defect formation. By invoking heat accumulation effects [18–21], large numbers of laser pulses (typically in the range of 10^3–10^7) at repetition rates in the kHz to MHz range were also used to produce large (a few microns in diameter) structures, but primarily inside transparent materials. Nevertheless, the machined structure in these cases is always associated with an undesired surrounding heat affected zone.

Very recently, Kerse et al. [22] demonstrated a novel high-throughput ablation concept using a multiple pulse structuring technique. The basis of this idea is to eliminate the heat of the material generated by a laser pulse by removing any ablated materials (debris) with the next pulse, before heat diffusion occurs. This implies that machining with moderate energy pulses, which will eventually excite large volumes of material per pulse (effectively, high ablation rate per pulse), can still be used to process material without creating a heat affected zone, provided suitable pulse trains

(i.e., at very high repetition rate in few hundred MHz range) are employed. This technique is thus very useful for high-speed processing, especially for thermally sensitive materials. Indeed, the authors have demonstrated virtually damage-free ablation of brain tissue at a rate of 2 mm^3 per minute using a 432 MHz intra-burst repetition rate, 27 kHz burst repetition rate, and 16 µJ pulse energy.

In contrast to the laser based surface structuring technique, when laser beams are focused inside any transparent material, as shown in Fig. 6.2a, a very localized material phase change may be triggered depending on the excitation conditions defined by the laser parameters and the focusing arrangement. The basic material excitation mechanisms are essentially the same as those used in the case of a surface structuring technique. However, the material relaxation scenarios are different. Nevertheless, the resultant phase transformation can be in the form of either an increase or decrease in the density or refractive index, with respect to the native values of the material. This is the basis of a *laser based bulk structuring technique*. Since the light-matter interaction zone can be flexibly placed anywhere within the material, the above technique is applicable to numerous applications requiring structuring in 3D space. For instance, Glezer et al. [23] demonstrated data storage applications by suitably machining (using single 100 fs laser pulses focused through a 0.6 NA lens) void-like structures as small as 0.008 µm^3 inside several transparent materials including glass, $LiNbO_3$, and polymer, as shown in Fig. 6.2b. Based on the laser induced localized material modification, especially the increased refractive index structure, direct writing of waveguide structures has been demonstrated for emerging technologies including quantum photonics [10, 24]. An illustrative image of waveguide writing is shown in Fig. 6.2c, where either the sample or the focused laser beam can be continuously translated along the desired direction within the material in order to realize waveguides in 3D. A propagation loss down to 0.1 dB/cm has been achieved using laser written waveguides in glass [25–28]. Similarly, localized increased refractive index structures have also been exploited in the fabrication of optical components including couplers and splitters [29, 30], volume Bragg gratings [31], diffractive lenses [32], and waveguide lasers [33]. Note here that above-mentioned demonstrations were based on point-like structures, and were facilitated primarily by either a tight focusing geometry, or by using a low pulse energy close to the corresponding material modification threshold value. Although the dimensions of bulk structures can be down to sub-diffraction sizes, as in the above examples, the scalability of such structures is questionable. For instance, if the laser pulse energy is increased, an axially elongated structure with an almost non-uniform shape may be obtained inside most transparent materials [34]. Such phenomena may be even more pronounced when loose focusing geometries are involved. Figure 6.2d shows a typical elongated microstructure with non-uniform index modification (negative and positive changes in the refractive index at the beginning and the end of the structure, respectively) produced in glass using femtosecond laser pulses with loose focusing (0.5 NA objective lens) geometry. This structure elongation is mainly attributed to the involvement of non-linear propagation dynamics of Gaussian beams along with the optical breakdown processes [35]. For instance, when operating at levels significantly above the material breakdown (laser intensity dependent process) threshold regime,
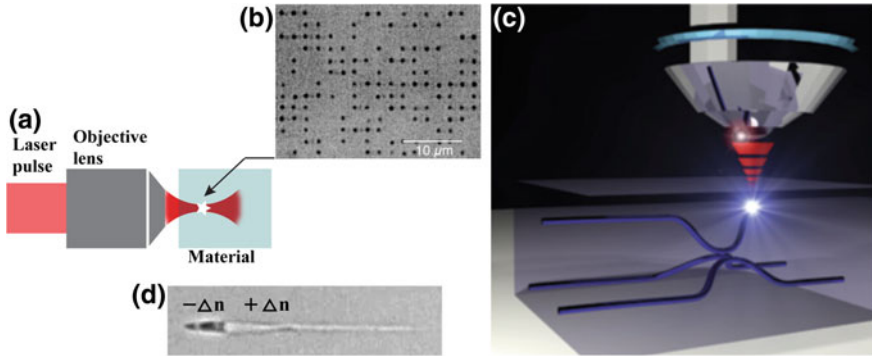
Fig. 6.2 Laser-based bulk structuring technique: **a** Typical machining scheme, showing laser pulse focusing inside a transparent material through an objective lens. **b** Optical micrograph of single pulse induced voids acting as data bits inside fused silica glass for data storage applications [23]. **c** Illustration of laser writing of waveguide structures produced by traversing the sample continuously during irradiation [25]. **d** Optical micrograph of a typical elongated structure inside glass produced using high energy femtosecond laser pulses. The regions with positive and negative changes in the refractive index of the structure are indicated as $+\Delta n$ and $-\Delta n$, respectively [34]. Reproduced with permission from The Optical Society of America (OSA), Laser Focus World, and American Physical Society (APS)

the self-focusing phenomenon (laser power dependent process) may come into the picture, but can be suppressed to some extent by using a tight focusing geometry (such as by using an objective lens with an NA close to one). From a fundamental viewpoint, such self-focusing concentrates light (like a positive lens) due to Kerr effect, that results in plasmas (act like negative lens) that can defocus the beam. This focusing-defocusing cycle continues over some beam propagation distance, producing a self-guided elongated plasma channel in a process referred to as filamentation. Note that the spatio-temporal dynamics associated with the filamentation process is very complex (difficult to control) and hence scalable material processing involving such nonlinear laser beams is limited. Nevertheless, filamentation-based elongated structuring of transparent materials can still be used for potential applications such as deep drilling and cutting [35–40].

By exploiting the filamentation process in loose focusing geometries (using an objective lens of 0.5 NA), and also in multiple pulse illumination schemes, Sudrie et al. [31, 34] first successfully produced extended, but non-uniform, structures (up to 80 µm long and a few µm in diameter) in fused silica glass using femtosecond laser pulses (160 fs pulse duration, 800 nm wavelength, and 7.8 MW power at 200 kHz repetition rate). Ultraviolet (UV) filaments were also exploited to facilitate elongated structuring of $LiNbO_3$ [41] and fused silica [42]. Shah et al. [43] successfully drilled straight hollow channels (≥ 1 mm long with aspect ratios up to 10) in glass in ambient air, and Varel et al. [44] drilled long microchannels in quartz in vacuum conditions. Even in tight focusing conditions where a substantial reduction of nonlinear beam propagation effects is expected, femtosecond laser beams can undergo filamentation process and can induce elongated, yet very narrow structures inside transparent materials. For example, Kydryashov et al. [45] first reported fabricating
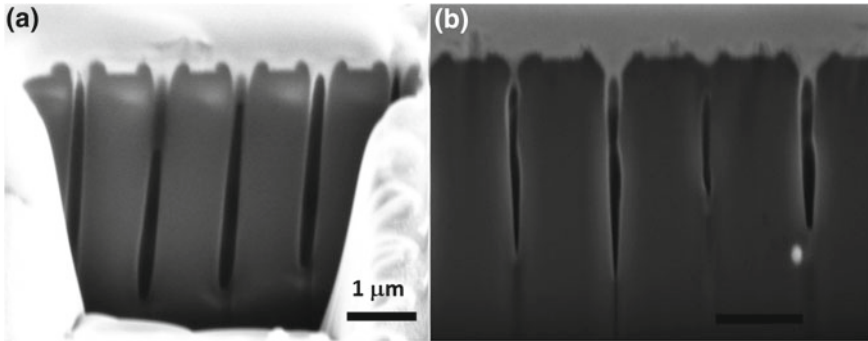
Fig. 6.3 Gaussian laser beam based nanochannel formation in Corning 0211 glass using a single femtosecond laser pulse (600 fs pulse duration, 1053 nm wavelength, and a fluence of 67 J/cm^2). Cross-sectional SEM images of structures machined on **a** reverse surface, and **b** front surface [15]. Reproduced with permission from OSA

1 µm long and 100 nm diameter hollow channel-like structures connecting to the front surface of a sapphire specimen using a single femtosecond laser pulse (600 fs pulse duration, 1053 nm wavelength, and nearly 2 W power). They also reported similar observations inside glass. White et al. [46] produced nanochannels less than 500 nm in diameter and with lengths up to 12 µm connecting to the front surface of fused silica glass materials using a single femtosecond laser pulse (200 fs pulse duration, 800 nm wavelength, and nearly 1–3 µJ pulse energy), whereas Herbstman et al. [15] demonstrated nanochannels between 150 and 240 nm in diameter with lengths up to 8 µm on both the front and reverse surfaces of Corning 0211 glass using a single femtosecond laser pulse (600 fs pulse duration, 1053 nm wavelength, and fluence of 67 J/cm^2), as shown in Fig. 6.3. It was also observed that the structure quality depends on the focusing geometry. For instance, channels with parallel walls were obtained in the case of reverse surface machining (see Fig. 6.3a), and tapered channels were observed for front surface machining (see Fig. 6.3b).

From a fundamental viewpoint, several mechanisms were proposed behind the formation of extended nanochannels in transparent materials using a single femtosecond laser pulse. The first mechanism, proposed by Kudryashov et al. [45], refers to short wavelength Bremsstrahlung radiation from hot dense electron-ion plasma, which can propagate and excite longitudinally beyond the skin depth (typically a few tens of nanometers) inside the material. This can cause melting over a longitudinally extended zone. During the relaxation phase, matter might have ruptured, thus leaving behind an empty zone referred to as a channel, within the material. More realistic mechanisms are based on filamentary propagation of Gaussian beams that cause longitudinal extension of focal zones, and hence extended scale ablation resulting in nanochannels, in the considered transparent materials. Spherical aberration (a linear phenomenon) can also act towards extending the focal zone longitudinally. This is because, compared to the central part of the normally considered Gaussian beams, marginal rays with large incidence angles deviate more at the air-glass interface in

the case of a tight focusing geometry. For example, Kanehira et al. [47] produced structures that were nearly 200 μm long embedded with quasi-periodic nanovoids 380 nm in size, and with a pitch of 1.7 μm, in a 900 μm thick Borosilicate glass specimen using 250 laser pulses of 10 μJ energy, whereas Sun et al. [48] and Song et al. [49] reported having observed similar effects. Although the underlying physics are yet to be discovered, Kanehira et al. attributed the mechanism of forming extended structures to both self-focusing and spherical aberration. In addition, those authors also presented some arguments in favor of standing electron plasma wave causing periodic nanovoids. In short, the leading edge of a high intensity laser pulse can, by itself, produce carrier plasmas inside glass that can interact with the trailing part of the pulse, thereby forming an electron plasma wave. When this plasma wave propagates into a region with a large plasma density gradient, it will be reflected and interfere with the forward travelling wave, thereby creating a standing wave pattern. As a result, the free carrier density distribution might be modulated, triggering periodic microexplosions and thus resulted into a periodic nanovoid structure. To summarize, ultrafast Gaussian laser beams have been shown to be capable of machining not only near-spherical (increased refractive index structures and voids), but also elongated sub-micron diameter channel-like structures inside several transparent materials including glass and sapphire on single-pulse and multiple-pulse irradiation basis.

6.2.2 Near-Field Approach

It has been demonstrated that ultrafast lasers associated with far-field focusing arrangements are capable of machining very fine structures down to few tens of nanometers on or inside most technologically relevant materials, as discussed in the previous section. In these cases, the spatial resolution of the machining is primarily dictated by the beam focusing strategy (linear) in conjunction with the applicable nonlinear light confinement processes. Meanwhile, several novel approaches based on near-field optical phenomena have been demonstrated for nanoscale material processing, but (so far) have been strictly limited to the surface of any samples. For instance, tip-based machining approaches [50] combined with either atomic force microscopy (AFM) [51] or near-field scanning optical microscopy (NSOM) [52], have produced spatial machining resolutions down to 30 nm. Here, the strong light localization near the tip causes a change in the thermo-mechanical properties of the material, or even ablation at a very confined spatial scale under the tip. Since these techniques rely on the near-field concept, the working distance is extremely short (a few tens of nanometers). Therefore, an active feedback control system is often employed to maintain the fixed distance between the sample and the tip, and hence to obtain uniform material processing.

Micron size spherical particles (instead of tips) are also exploited for sub-wavelength light localization, and show strong potential for use in fundamental and technological applications including optical nano-sensing [53], nano-surgery [54, 55], and nanoscale material processing [55–60]. Light transmitting through a dielec-

tric microsphere tends to emerge with a high intensity photon flux directly behind the sphere. The birth of the high intensity jet-like beam lies with the fact that a microsphere can be treated as a mesoscopic scattering particle for visible radiation, which means it can scatter light strongly in the forward direction. This scattered light then interferes with the transmitted light refracted through the sphere and produces a highly localized light wave known as "photonic jet". The primary features of photonic jets are as follows: (a) Strong transverse light localization maintained over several wavelengths along the longitudinal direction. For instance, the jet diameter can be as small as just a few hundred nanometers, and the jet length can be extended up to a few micrometers. It has also been shown that the length scale of the photonic jet can be improved further by using a multilayer dielectric microsphere [61, 62], a micro-ellipsoid [63], a liquid filled hollow micro-cylinder [64], a hemispherical cell [65], and a micro-axicon [66]. (b) The spatial distribution and intensity of a photonic jet depend primarily on the sphere diameter and the refractive index contrast between the sphere and its surrounding medium. Most importantly, the peak intensity of the photonic jet can exceed the ablation threshold level for most technologically relevant materials.
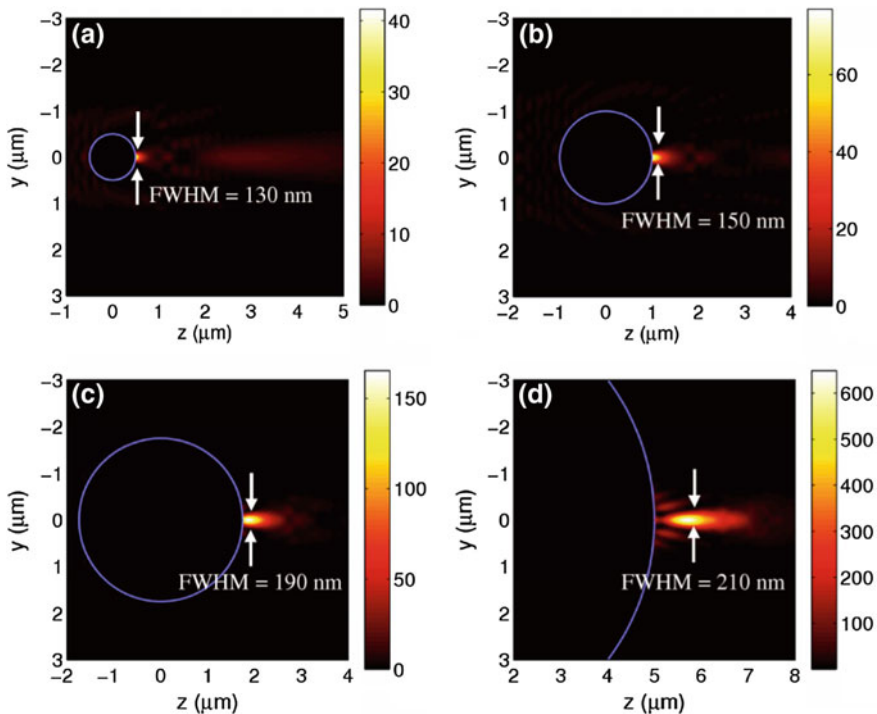

Fig. 6.4 Simulation results: photonic nanojets with a wavelength of 400 nm, produced by microspheres with a refractive index of 1.59 at diameters of **a** 1, **b** 2, **c** 3.5, and **d** 8 μm [53]. Reproduced with permission from OSA

Figure 6.4 shows simulation results for a typical photonic jet, demonstrating its spatial characteristics as a function of sphere diameter [53]. A linearly polarized light wave (polarization direction is perpendicular to the sheet) with a 400 nm wavelength is incident (along the z-direction) on spherical particles that have a refractive index of 1.59 in the ambient environment. The smallest lateral size photonic jet (which eventually dictates the machining spatial resolution), which has a full width at half maximum (FWHM) of 130 nm, was obtained for a 1 μm diameter sphere, as seen in Fig. 6.4a. The jet size increases with increasing sphere diameter. Nevertheless, the possibilities of confining light below the diffraction limit and tuning the beam profile as a function of sphere dimensions, have generated some research interest in the field of nanoscale material processing.

For example, Lu et al. [56] initially reported Si nanostructuring using laser (pulse durations ranging from 150 fs to 23 ns and wavelengths ranging from 248 nm to 800 nm) irradiation through microspheres. Huang et al. [59] demonstrated nanocraters on Ni film using the same technique, whereas Zhou et al. [60] reported nanoscale crater formation on a glass surface. In this last case, a monolayer of 1 μm diameter silica spheres was first deposited on a glass surface, after which a laser pulse (800 nm, 100 fs) was focused (spot size of 5.4 μm) on the microspheres. This resulted in nanocraters just below the spheres.

SEM image of craters and an AFM line profile of a typical crater are shown in Fig. 6.5a, b, respectively. The lateral size (200–400 nm) of the craters were also observed to be linearly scaled with the laser fluence, as illustrated in Fig. 6.5c. These results clearly present novel opportunities for rapid, large-area, and nanoscale mate-
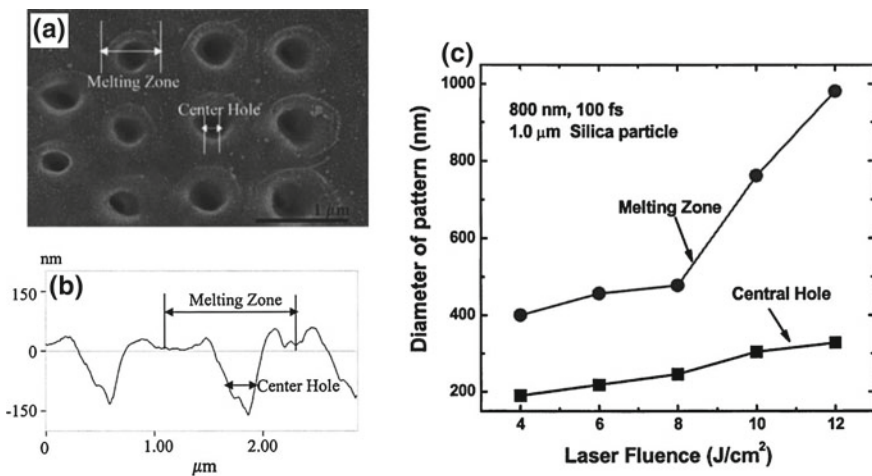

Fig. 6.5 a SEM images of photonic nanojet assisted nanocraters on glass surfaces. The laser pulses (wavelength of 800 nm, pulse duration of 100 fs, and fluence of 35 J/cm^2) pass through a monolayer of 1 μm-diameter silica spheres to form surface craters. **b** AFM cross-sectional line profile of a typical crater shown above. **c** Evolution of average crater diameter with respect to the laser fluence [60]. Reproduced with permission from AIP

rial processing. However, the above technique provides little freedom for designing and emplacing the nanostructures, as these elements are primarily dictated by the methods used to deposit the spheres on the relevant materials. To overcome this drawback, McLeod et al. [67] proposed a technique based on an optical trap [68, 69] that holds the microsphere in an aqueous environment. More specifically, zero-order Bessel beams [70, 71] were employed to trap a polystyrene microsphere near the substrate (to be machined), by suitably balancing the scattering force imposed on the sphere by the beam with the counter forces, such as electrostatic repulsion between the sphere and the substrate. The microsphere was therefore self-positioned (without any help of feedback system) at a distance of about 50 nm from the substrate. In this way, the authors demonstrated direct writing of individual as well as continuous structures with lateral sizes down to 100 nm on polyamide films. The self-positioning mechanism also facilitates machining of non-uniform surfaces, and the technique also has the potential to be used for parallel writing using adaptive optics [71–74] such as by trapping several spheres at the same time, followed by laser illumination for nanoprocessing.

6.2.3   Alternative Technology to Laser Machining: Focused Ion Beam (FIB) Machining

With its state of the art fabrication capability down to 10 nm, the focused ion beam based nanofabrication technique [74–77] is mostly utilized for the fabrication (primarily on surface) of plasmonic components, X-ray optics, photonic crystal fabrication, and other such applications where high fabrication resolution and accuracy are important. However, laser machining has the potential to beat the FIB technique in two areas. First, in terms of fabrication resolution, Joglekar et al. [13] have already demonstrated surface craters with sizes down to 30 nm. Since this precision comes from the strength of nonlinear light-matter interactions, it can be predicted that with recently discovered ultrashort laser pulses (such as few cycle laser pulses) and spatiotemporal engineering concepts [78], the fabrication resolution can be further reduced to just a few nanometers in the future. Second, in terms of fabrication depth, the laser (normally considered Gaussian spatial profile) machining technique is already on a par with the FIB technique. For instance, FIB can only machine a few microns deep inside some technologically relevant materials, such as TiO_2, as shown in Fig. 6.6 [75].

The figure shows an SEM cross-sectional image of a typical photonic crystal, which consists of an array of 50 nm diameter nanochannels with an aspect ratio of 10, machined using FIB fabrication, for visible light manipulation. In contrast, machining of channels that are just a few tens of nanometers wide and up to 10 μm long has been demonstrated in glass using Gaussian laser beams. Furthermore, there is a significant increase in fabrication depth [up to a millimeter (mm)] when using zero-order Bessel laser beams, which will be discussed in the final section of this chapter. Note that even though the recent machining demonstration using the FIB
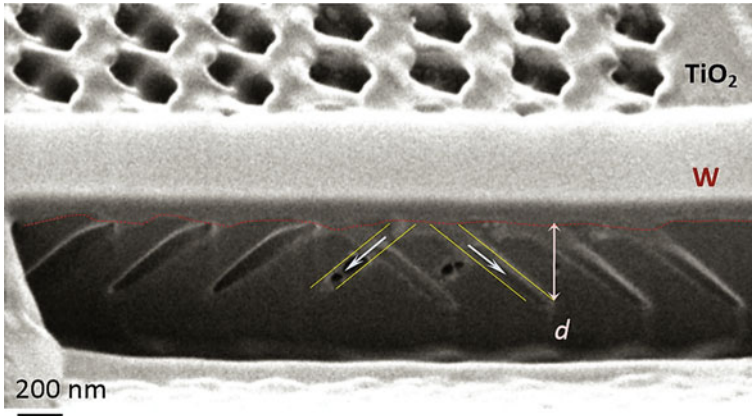
Fig. 6.6 FIB fabrication results: SEM cross-sectional image of a 3D photonic crystal in TiO_2 produced using FIB. The photonic crystal consists of an array of nanochannels (FIB fabricated) of diameter of 50 nm, and an aspect ratio of 10 [75]. Reproduced with permission from OSA

technique represents the current state of the art, the fabricated structures still cannot be integrated completely in the volume. In contrast, it can be foreseen that a fabrication technique involving a laser beam in ambient air (instead of the vacuum environment required for FIB) will emerge in the future, and the final section of this chapter on laser machining using non-diffractive beams provides a potential pathway to the realization of this goal.

6.3   Hybrid Approach

Direct fabrication techniques involving ultrafast Gaussian laser beams can achieve super-resolution structures, but the scalability of the structure diameter is questionable, as discussed in the previous section. In particular, since the direct fabrication of large diameter (more than few microns) structures (especially hollow-like) is extremely difficult, hybrid material processing approaches, such as those discussed below, have been developed. The first hybrid approach relates to single-step processing i.e. laser ablation of materials that are essentially transparent to incident light, in the presence of an aqueous environment in order to facilitate removal of ablated particles. The second approach relates to two- and three-step processing i.e. laser induced material modification followed by chemical etching and as-needed heat treatment. The underlying mechanisms and technical capabilities of such techniques are also discussed below.

6.3.1 Single-Step Processing: Laser Machining in Suitable Environment

Laser machining of transparent materials in the presence of a suitable environment using the multiple laser pulse irradiation scheme has been shown to be very effective for fabricating hollow channels, without any need of post-fabrication processes. Long straight microchannels were machined in transparent materials such as quartz in a vacuum environment, which facilitated the removal of ablated materials [44]. The use of a liquid environment (which is in contact with the machining surface) offers more flexible microchannel fabrication in terms of length and shapes. Different liquids such as water, methanol, ethanol, and isopropanol were evaluated for this process, eventually leading to the conclusion that low viscosity fluids are better candidates for hybrid machining techniques [79]. Water assisted machining techniques have been shown to have great potential for producing arbitrarily shaped hollow channels in transparent materials. The methodology of the machining technique shown in Fig. 6.7a, can be understood as follows: a femtosecond laser pulse is first focused (through the material) at the reverse surface of a transparent material placed in contact with water, after which the laser focal point can be translated inside the material along the chosen trajectory in order to obtain arbitrarily shaped 3D hollow channels.

For example, Li et al. [80], the inventors of the water-assisted machining technique, successfully fabricated 4 μm diameter microchannels with aspect ratios of up to 50 in silica glass at an effective sample translation speed of 0.3 μm/s using an objective lens of 0.55 NA. Figure 6.7b shows an optical micrograph of a typical continuous square-shaped hollow microstructure machined in this way. Using a similar technique and focusing geometry, Iga et al. [81] drilled straight 2-μm-diameter microchannels with aspect ratios of up to 325. Later, Hwang et al. [79] enhanced this method by adding ultrasonic wave agitation in order to machine straight and curved 3D channels with diameters on the order of tens of microns (see Fig. 6.7c, d), and aspect ratios of around 40 in glass at a translation speed of up to 30 μm/s using an objective lens of 0.42 NA. In addition, Ke et al. [82] successfully fabricated very long channels (>200 μm) of very small diameter (<700 nm) and aspect ratios of up to 1000.

Although technical exploitation of the liquid assisted machining technique has been very successful, the underlying physical mechanisms involving laser induced plasma generation, bubble generation and expansion, and the generation and expansion of shock/pressure waves are very complex, and not yet fully understood. However, the essential physics of this technique can be elucidated as follows: the laser pulse focused on the reverse surface of the sample in contact with a liquid can trigger an optical breakdown of the sample, thereby causing matter ablation. Simultaneously, part of the laser pulse energy can also be absorbed by the liquid such as water. This causes rapid heating (typically at the rate of 10^{10} K/s [82]) and water vaporization, thereby creating bubbles inside the water. Such bubbles create a liquid flow, assisted by the thermal convection processes, that carries away the debris. This process is followed by the immediate inflow of the surrounding water into the ablation site. As
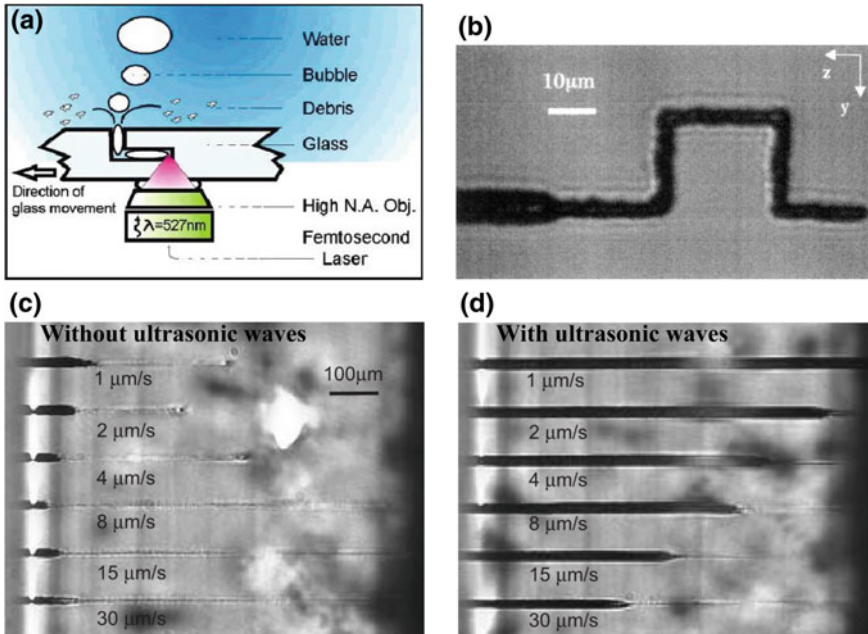
Fig. 6.7 Water-assisted micromachining results in glass: **a** Scheme of laser machining in liquid environment [82], **b** optical micrograph of a continuous, square-shaped hollow microstructure fabricated in glass using this machining technique [80]. Optical micrographs of microchannels machined without (**c**) and with (**d**) the assistance of ultrasonic waves [79]. Reproduced with permission from The American Chemical Society (ACS), OSA, and Springer

the laser focal point moves inside the sample to illuminate the fresh ablation site, the "sample ablation-bubble generation—bubble and debris evacuation" processes continue. Gradually, a hollow channel shaped structure appears.

In a broader sense, the large number of bubbles generated and their fast entrainment through the channels leads to rapid debris evacuation inside the channels. This necessitates the proper selection of laser parameters and liquids for the machining of high quality channels. The rate of bubble expansion and collapse needs to be balanced with the laser repetition rate, which has been normally limited to a range of just a few kHz, while remembering that the bubble lifetime in such ablation conditions is in the order of a millisecond. Thus, any minor fluctuation in laser energy would lead to different bubble dynamics that would interrupt the channel evolution process. In addition, laser focal point scanning has to be maintained precisely at the ablation site (which moves with each pulse) in order to avoid channel clogging. Note here that the water flow inside micron and sub-micron size channels, which is essential for realizing long channels, is assisted by capillary forces that impose no obvious limitations on long hollow structure machining.

6.3.2 Multi-step Processing: Laser Irradiation, Followed by Chemical Etching and Heat Treatment

As discussed in the previous section, processing of transparent materials in a single-step, such as by using water-assisted machining technique, is useful for obtaining long, arbitrary shapes and hollow structures with lateral sizes down to few hundred nanometers. However, since the structure/channel wall quality is observed to be poor, reservations exist regarding their usage in technological applications. Multi-step processing techniques based on photo-physical or photo-chemical reactions and selective chemical etching are often considered as ways to tackle the above-mentioned issue [83, 84]. The methodology of such multi-step processing technique can be understood as follows: femtosecond laser pulses (tens of nanojoules to a few microjoules of pulse energy at high repetition rates, typically in the kHz to MHz range) are first focused at a certain position inside the material, after which the focal point is scanned along a pre-designed path in order to induce soft material modifications. Note that the laser irradiation path must connect at least one of the sample surfaces. After laser irradiation, the sample is placed inside a chemical compound mixture consisting of hydrofluoric and sulfuric acids in order to etch out the laser modified material. Depending on the molar concentration of the acids used, the etching time may vary from a few minutes to a few hours. One of the advantage associated with this technique lies with the use of very low (by at least one order of magnitude) energy pulses compared to the single-step, ablation-based machining methods. Marcinkevicius et al. [85] fabricated an H-shaped 3D structure of interconnected 12 μm wide hollow channels with arbitrary angles of interconnection inside silica glass using this technique. Combining focal spot engineering with a two-step machining technique, Cheng et al. [86] varied the beam focal depth to machine hollow channels with arbitrary cross-sections in glass.

With an aim towards enhancing the potential of such two-step processing techniques, special photosensitive materials, such as Foturan glass, are being considered for technological applications. For such glasses, the etching rate of the laser-exposed region is significantly enhanced compared to the unirradiated region. However, the processing technique requires multiple steps. After laser irradiation along the desired path, the photosensitive material is annealed (up to few hundred centigrade), after which the sample can be treated with chemicals to etch out the laser-modified region. Following this approach, Masuda et al. [87] and Sugioka et al. [88] fabricated a microfluidic device based on Foturan glass that contains a movable plate inside the channels for controlling the flow direction of certain reagents, as shown in Fig. 6.8.

However, there are several undesired effects that are associated with above-mentioned multi-step processing techniques. These include (i) Channel tapering: since the exit point of a laser modified zone is more exposed to chemical etching than the interior parts, tapering (longitudinally) occurs in the resultant channels. The tapering effect is stronger as the laser modified zone decreases in lateral size (below a few tens of microns). Nevertheless, this effect can be neglected when fabricating channels that are just a few hundred microns in diameter, as are often used for
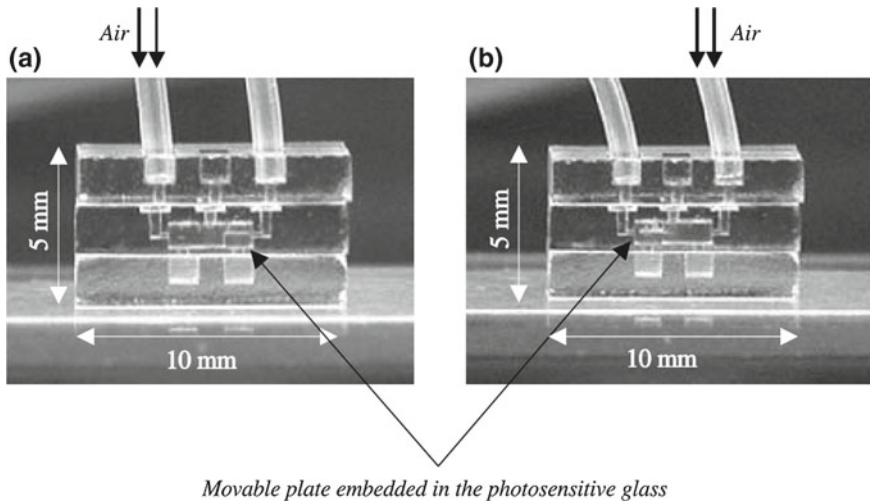
Movable plate embedded in the photosensitive glass

Fig. 6.8 Microstructures fabricated inside photosensitive glass using multi-step processing techniques. A microfluidic device prototype with a freely movable microplate that can switch the flow direction of reagents is shown. The movable plate inside the glass was realized by laser structuring followed by heat treatment and chemical etching. **a** By infusing compressed air from the left opening of the top part, the microplate moves to the right side. **b** As compressed air is infused from the right opening of the top part, the microplate moves to the left side [88]. Reproduced with permission from Springer

lab-on-a-chip or bio-chemical applications [86, 88]. A novel possibility for overcoming the tapering effect was explored by Chaitanya et al. [89]. In this technique, the laser modification pattern was designed like double cones facing each other so that after the chemical etching treatment, the resultant channel becomes cylindrically shaped. (ii) Complex integration: chemical etching processes that rely on the chemical selectivity of the laser modified material do not differentiate well between soft material modification (basis of waveguide structure) and strong material modification. Therefore, simultaneously writing both waveguides and hollow channels for opto-fluidic applications is very challenging. In fact, when integrating microfluidics with optical waveguides, the waveguides are always written after the fabrication of the microfluidic components.

6.4 Non-diffractive Approach for Flexible Fabrication

The contemporary approach to material processing involves fabrication using optical beams that do not diffract while propagating from one point to the other, and which can attain both super-resolution (lateral sizes down to 100 nm) as well as longitudinally extended length scales (up to 1 mm). Being propagation invariant solutions

of Helmholtz equation, non-diffractive optical beams such as Bessel beams [70, 71] and Airy beams [89–92] have been advocated as potential candidates for advanced material processing. Such beams can ideally overcome diffraction and hence require an infinite amount of energy, which obviously means these beams cannot be realized in practice. However, quasi-diffraction free beams have been experimentally generated that retain their inherent beam characteristics (i.e., non-diffractive and self-reconstruction behavior [93, 94]) over limited propagation distance. Such beams are now being used in numerous applications in fields such as nonlinear optics [94–100], plasma physics [101, 102], material processing [103, 104], optical trapping [69, 105, 106], microscopy [107, 108], and atom guiding [109, 110]. From an application viewpoint, physical parameters such as the central lobe size and the corresponding intensity (specifically, the highest among all the surrounded lobes) of non-diffractive beams, are of the utmost importance. In this section, we focus primarily on the application of quasi-non-diffractive beams for fast and flexible material processing.

6.4.1 Zero-Order Bessel Beams

Durnin et al. [70] first studied solutions of Helmholtz equation and found Bessel type solutions that have electric field structures independent of the propagation distance. In a cylindrical coordinate system, the electric field structure of such a wave can be described as

$$E(r, \Phi, z) = E_0 J_n(k_r r) e^{i k_z z} e^{\pm i n \Phi},$$

where E_0 is a constant, r, ϕ and z are the radial, azimuthal, and longitudinal axes, respectively, k is the wave vector relating its radial component, $k_r = k \sin \theta$, and the longitudinal component, $k_z = k \cos \theta$, J_n is the nth order Bessel function of the first kind, and θ is the half-angle of the cone containing all the wave vectors (more explanation of this parameter is given in the following paragraph) that superimpose to form Bessel beams. When $n = 0$, the above equation is reduced to

$$E(r, z) = E_0 J_0(k_r r) \exp(i k_z z),$$

which defines the field structure of zero-order Bessel beams. Therefore, its corresponding intensity is proportional to $J_0^2(k_r r)$, clearly indicating concentric ring patterns with a central bright spot. Importantly, the central spot of this Bessel beam, which is equivalent to the focal spot of a Gaussian beam, does not diffract over the beam propagation distance. This unique property has made the beam of particular interest for high-aspect-ratio micro and nanostructuring applications.

   For the generation of zero-order Bessel beams, several methods have been proposed using passive components such as annular disk [70], axicon lens [110–113], static hologram [114] and dynamically reconfigurable hologram generated via spatial light modulator (SLM) [114–119]. Among these methods, a generation approach

Fig. 6.9 Zero-order Bessel beam characteristics and generation method: **a** Peak intensity variation along the longitudinal direction corresponding to Gaussian and BG beams that have central spot sizes of 1.8 μm. **b** Experimental arrangement for axicon lens-based Bessel beam generation along with a magnification system comprising two lenses (L1 and L2) and a spatial filter to produce high-quality and high cone angle zero-order Bessel beams
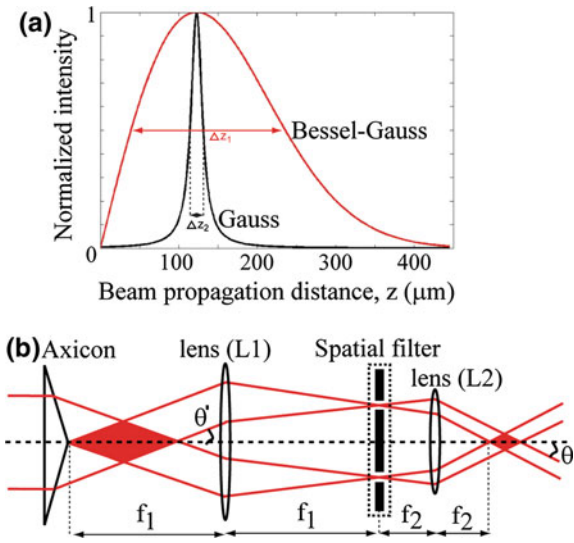
based on an axicon lens (a cone-shaped optical element) has attracted significant amounts of attention due to its ability to produce high throughput (nearly 100%) beam transformation (from Gaussian to Bessel beams) in an economical manner. In contrast, diffraction-based optical elements, such as SLM, suffer from typically below 50% beam transformation efficiency. When collimated monochromatic Gaussian laser beams with flat phase front are incident normally on an axicon with n_{ax} refractive index and α wedge angle (sometimes referred to as base angle), the beams deviate towards the main axis (along the beam propagation direction) with an angle θ' and overlap. This produces an interference effect that can be characterized as zero-order Bessel beams (sometimes referred to as Bessel-Gauss (BG) beams) of conical half-angle θ'. With pure geometrical optics considerations, Snell's law at the inclined face of an axicon gives rise to the following expression:

$$\theta' = \arcsin(n_{ax} \sin \alpha) - \alpha.$$

A quantitative comparison of the on-axis (central axis) intensities of Gaussian and BG beams with identical 1.8 μm spot sizes is shown in Fig. 6.9a. As evident from the figure, the longitudinal distance (non-diffracting length) for BG beams is nearly one order of magnitude longer than that for Gaussian beams. The mathematical description of BG beams generated by an axicon lens is usually based on Fresnel diffraction integral evaluated under stationary phase approximations [120]. The on-axis intensity $I(z)$ of BG beams thus produced at a distance z from the beam onset point (the axicon tip) can be expressed as follows [121]:

$$I(z) = 8\pi P_0 z \, \sin^2 \theta' / \lambda_0 w_0^2 \cdot \exp\left[-2\left(z \sin \theta' / w_0\right)^2\right],$$

where P_0 is the peak power of the laser beam incident on the axicon, λ_0 and w_0 are the wavelength and waist of the incident laser beam, respectively, and θ' is the conical half-angle of the experimentally generated BG beams. Note here that, compared to the BG beams in air, the conical half-angle θ' of BG beams in glass is reduced by a factor of n, the refractive index of glass, whereas the non-diffracting length Z_B gets lengthened by a factor of n. Interestingly, the size of the central core of BG beams does not change while propagating linearly in glass. However, according to Polesana et al. [122], the core size becomes reduced in cases involving the nonlinear propagation of Bessel beams in Kerr media.

From a technical viewpoint, although the use of an axicon has been observed to be very efficient for generating BG beams, the alignment of the illuminating beam over the axicon is very critical. Any off-axis and oblique-axis axicon illumination can easily aberrate the generated BG beams, thereby resulting in a checkerboard type pattern instead of a central spot with concentric rings. Additionally, typical axicon manufacturing defects, such as oblate tips, often modulate the on-axis intensity profile of BG beams. Of course, a methodology based on Fourier filtering can be adopted to obtain near-ideal BG beams. Another important issue, especially within the framework of Bessel beam-based material processing (which typically requires high-angle BG beams [121, 123]) concerns the direct applicability of an axicon lens alone. In fact, large base angle axicon lens are not suitable (and often commercially unavailable) for high cone angle BG beam generation due to large scale aberrations and pulse broadening effects that result from the large thickness of the axicon lens itself. Therefore, telescopic systems are normally employed in association with an axicon lens to produce BG beams of micron and sub-micron central core sizes, which eventually determines the fabrication resolution. A typical axicon lens based Bessel beam generation scheme is depicted in Fig. 6.9b, where a telescope consisting of lens L1 (of focal length f_1) and lens L2 (of focal length f_2) with a de-magnification factor of f_2/f_1 is employed. For example, when $\alpha = 0.5°$, $n_{ax} = 1.45$, $f_1 = 1$ m, and $f_2 = 20$ mm, a BG beam of conical half-angle $\theta = 12°$ can be obtained in air, with its onset position lying at the focal plane of the objective lens, L2. A spatial filtering arrangement [124] at the focal plane of lens L1 followed by the axicon lens was also employed to produce near-ideal BG beams. The spatial filter is mainly composed of a stopper that blocks undesired wave vectors lying inside the ring and an aperture that blocks undesired wave vectors lying outside the ring. This arrangement only allows passage of the wave vectors passing through the stopper-aperture based annulus region, and thereby ensures near-ideal BG beams at the focal plane of lens L2. Interestingly, recently, Dudutis et al. [125] discovered an application of modulated BG beams (i.e., with no spatial filtering) generated by an imperfect axicon lens, for initiating preferential cracks, leading to cutting of transparent materials.

Surface processing:

Exploiting their inherent properties, zero-order BG beams are shown to be useful for large-area, nanoscale surface processing. For the sake of comparison, a smaller spot (sub-micron size is needed for better fabrication resolution) can be obtained using a tight focusing geometry in the case of Gaussian beams. However, tight focusing of

Gaussian beams also results in shrinking the corresponding longitudinal depth to a few microns. Now, when laser processing over a large area ($\sim cm^2$) is required, maintaining a fixed distance between the sample and the laser focal point is a tedious job that would normally require an adaptive positioning control system, thereby adding complexity and expense to the manufacturing process. However, BG beams offer potential solutions to this problem. In ablation-threshold regime, the light-matter interaction zone involving primarily the BG central core can be defined and positioned with respect to the material to be processed in a more efficient way compared to comparable Gaussian beams. Note that the central core size of a BG beam is a function of its cone angle (a high cone angle corresponds to a small core size), while the longitudinal depth (non-diffracting length) of a BG beam is a function of the beam apodization (a large input beam size corresponds to a large depth of focus). Most importantly, since both the central core and the longitudinal depth of focus are essentially decoupled from each other, they can be independently controlled, which is an unusual characteristic when compared to Gaussian beams. These unique characteristics remove the stringent criteria of sample-beam positioning that is normally required for large-area processing.

Courvoisier et al. [126] demonstrated that the size and morphology of the structures machined on a glass surface using high cone angle Bessel beams ($\theta \sim 24°$) do not vary much over long distances (up to a few tens of microns), and Sahin et al. [127] successfully machined slits (see Fig. 6.10a) with widths down to 125 nm on a 25 nm thick gold film over glass using femtosecond BG beams ($\theta \sim 20°$). They also reported a prominent plasmonic resonance effect at wavelengths around 900 nm when using nanoslit arrays with 860 nm periodicity, as shown in Fig. 6.10b.

To summarize, large-area surface processing, especially of opaque materials in the ablation threshold regime, can be very productive when using high cone angle BG beams. While this has opened a potential route to machining plasmonic, metasurface structures, such a technique would face scaling restraints in terms of the machined
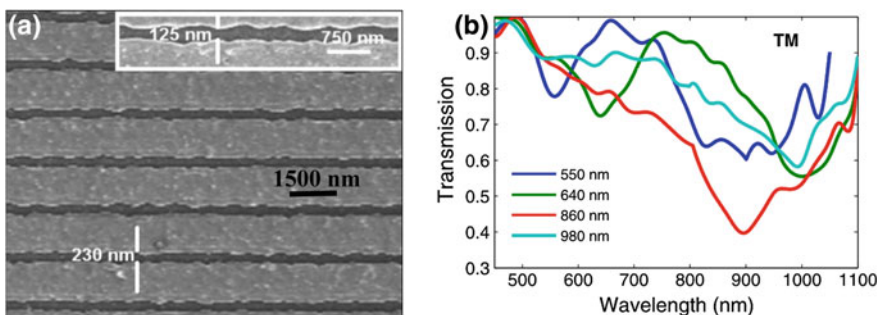

Fig. 6.10 **a** SEM image of nanoslits machined on 25 nm thick gold coated over glass using zero-order BG beam. The darker regions of the image are ablated stripes. The corresponding plasmonic response is shown in (**b**), depicting the transverse magnetic transmission spectra corresponding to four nanoslit arrays with periodicities of 550, 640, 860 and 980 nm cases [127]. Reproduced with permission from AIP
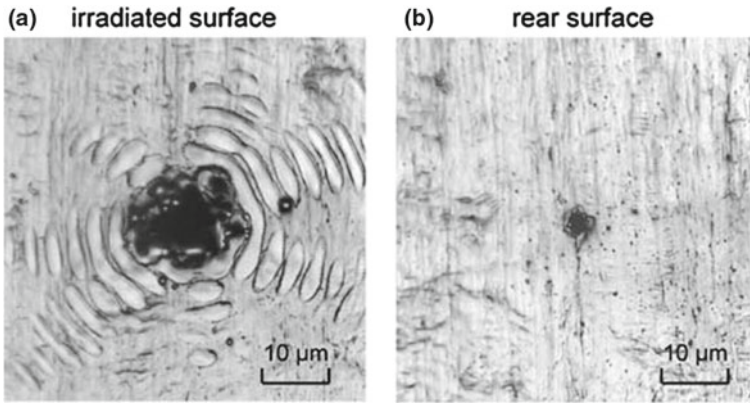
Fig. 6.11 SEM surface profile images of a hole drilled into a 20 μm thick stainless steel sheet using a BG beam (100 pulses of 20 J/cm² fluence). **a** Front surface profile, and **b** rear surface profile [128]. Reproduced with permission from Springer

structure size. For instance, when high energy Bessel pulses are employed in order to obtain large structures, a signature mark of concentric ring-shaped structures is obtained, as shown in Fig. 6.11. In fact, these results (as depicted in Fig. 6.11) represent one of the earliest studies by Matsuoka et al. [128] on BG beam machining. SEM surface profile images of a hole drilled into a 20 μm thick stainless steel sheet using a BG beam (100 pulses of 20 J/cm² fluence) clearly show that ring patterns are only visible on the front surface of the material. This is because material ablation occurs over the whole region exposed by several outer rings of BG beams, exceeding the ablation threshold fluence. Nevertheless, this ring (instead of point) structure is, in general, an undesired effect that can degrade the quality of high-density structures.

He et al. [129] proposed a technique based on tailored BG beams to address the issue of supplementary, yet unwanted, ring-type surface structuring. The beam tailoring technique followed by the authors was primarily based on the Bessel beam generation method of Durnin [70] using an annulus ring coupled with a lens. In the present case, a binary phase $(0 - \pi)$ plate consisting of numerous concentric annular zones was used to replicate the function of annulus rings. Each annular zone creates a BG beam of a certain cone angle that causes all the generated BG beams (by several annular zones) to lie together and interfere at the same point, which is defined by the axicon lens. The key to this technique lies with the phase tuning of individual annular zones that achieves constructive interference only at the Bessel central core positions and destructive interference in the region of outer lobes of all the generated BG beams. This permits a BG beam with a super-intense central core and highly suppressed outer lobes to be generated. When employed for material processing, such a beam can be expected to produce high-quality structures.

He et al. [129] produced such tailored BG beams using a custom designed phase plate for processing of Si using 65 fs laser pulses at a wavelength of 1.5 μm (to which Si is transparent) at a 1 kHz repetition rate. Longitudinal cross-sectional images of
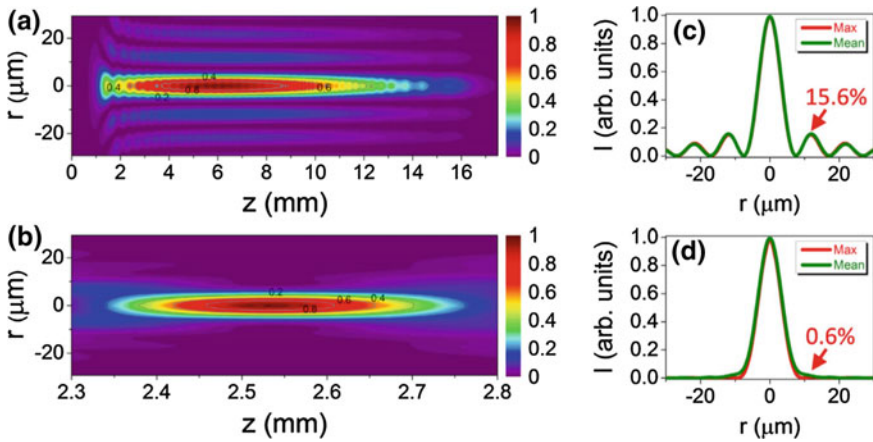
Fig. 6.12 Spatial characteristics of conventional and tailored BG beams. Longitudinal cross-sectional profiles for conventional (**a**) and tailored (**b**) BG beams are shown. The radial intensity profiles corresponding to conventional (**c**) and tailored (**d**) BG beams are also shown [129]. Reproduced with permission from Nature Publishing Group (NPG)

both conventional and tailored BG beams are shown in Fig. 6.12a, b. The radial peak intensity profile for the beams, as shown in Fig. 6.12c, d, clearly indicate that the side-lobe intensity for the tailored BG beam is suppressed to merely 0.6% compared to 15.6% for the conventional BG beam. Note that in both cases, the central core size was 6 μm. The potential use of beam tailoring for the machining of near-parallel channels in 50–100 μm thick Si, with no unwanted features around the channel opening, was demonstrated using a multiple pulse irradiation scheme (limited to a few hundred laser pulses per channel), as shown in Fig. 6.13a–f. From a quantitative view point, the Gaussian beams produced tapered vias/channels with front surface diameters of 20 μm and aspect ratios of less than 3, as can be seen from the SEM cross-sectional image of the channel shown in Fig. 6.13a. The conventional BG beams produced 5 μm diameter near taper-free vias with aspect ratios around 10 (see Fig. 6.13b). However, the applications of such vias are limited due to undesired surface damage caused by the characteristic concentric lobes of BG beams. In contrast, tailored BG beams produced a clean structure (with no additional damage) with characteristics similar to that of a conventional BG beam (see Fig. 6.13c). Figure 6.13d–f show the SEM cross-sectional, front, and rear surface 2D array images of through holes produced in 100 μm thick Si substrates by tailored BG beams.

Volume processing:

The potential application of zero-order BG beams to the machining of sub-micron scale surface features is clearly evident from the earlier paragraphs. Here, we discuss how BG beams are useful for controlled volume fabrication. In the context of BG beam volume interactions with transparent materials such as glass, it is important to note here that (analogous to Gaussian beams), BG beams also suffer from nonlinear
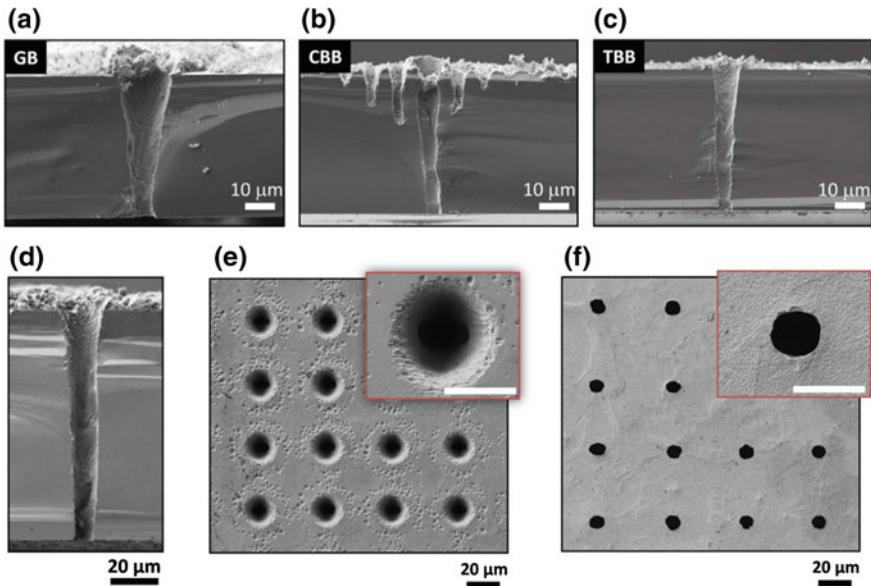
Fig. 6.13 Experimental results for through Si hole fabrication using laser beams with several spatial profiles. SEM cross-sectional profiles of through holes drilled in a 50 μm thick Si substrate using **a** Gaussian, **b** conventional BG, and **c** tailored BG beams are shown. **d–f** SEM cross-sectional, front, and rear surface images of two-dimensional (2D) array of through holes produced in 100 μm thick Si substrates by the tailored BG beam, respectively. The scale bars in the insets of **e** and **f** are 5 μm [129]. Reproduced with permission from NPG

effects, including the Kerr effect and the plasma defocusing effect, while they are propagating in the medium. Yet, it has been observed that BG beams are more robust to nonlinear distortion than Gaussian beams over a broad range of experimental conditions [97, 123]. Nevertheless, three different Bessel beam propagation regimes in Kerr media have been observed: weakly nonlinear Bessel filamentation, unsteady Bessel filamentation, and steady Bessel filamentation [97]. The most important case in the context of material processing refers to steady Bessel filamentation, where an extended plasma column of near-uniform density can be achieved, and where a significant level of energy absorption may occur inside the medium, especially when the plasma number density is above 10^{18}/cm^3. Experimentally, such a regime can be achieved in a certain parametric window of laser energy, pulse duration, and Bessel cone angle. In a broader sense, high cone angle BG beams normally produce high electron densities (close to the corresponding critical density) and therefore cause a higher level of energy deposition inside the medium, when compared to low cone angle BG beams. In a medium such as glass, even with low-level excitation (employing a low cone angle BG beam), soft material modification (in terms of positive changes in the refractive index) can be obtained, as reported by Marcinkevicius et al. [130], who were the first to demonstrate wave-guiding with low loss and birefrin-

gence effects in BG beam induced structures in glass. However, structure size and uniformity could not be maintained when the laser energy increased. In fact, one such (multiple pulse irradiation regime) case led to periodic damage structures, as observed by Gaizauskas et al. [98], who attributed BG beam induced structures to an unsteady Bessel filamentation process. Bhuyan et al. [131] also observed similar behavior when machining glass using femtosecond BG beams ($\theta = 7°$).

In brief, low cone angle BG beams normally induce a soft positive refractive index change ($\sim 10^{-4}$–10^{-3}), even though the structure size is not scalable solely on the basis of laser pulse energy. A typical example of femtosecond (60 fs) laser-driven positive index structures in fused silica glass using single pulse and multiple pulse (100 pulses at 1 kHz repetition rate) irradiation schemes is shown in Fig. 6.14a, b. A novel approach to single pulse machining involving low cone angle BG beams and exploiting the temporal engineering concept [78] demonstrated by Bhuyan et al. [132] provides additional control over the structural characteristics of material modification. Figure 6.14c shows a phase contrast microscopy (PCM) image of a single picosecond (4.7 ps) pulse induced negative index structure, such as a void inside fused silica glass. The impact of pulse duration (from 60 fs to 5.7 ps) on material processing was therefore studied and a gradual change in refractive index from positive to negative is clearly evident from the PCM images of single pulse induced structures in glass using BG beams ($\theta = 8.3°$, pulse energy of 4.1 µJ), as shown in Fig. 6.15a. A longitudinal cross-sectional profile of the BG beam is also shown in the top of this figure. A parametric window in the energy-pulse duration framework is shown in Fig. 6.15b. Here, the highlighted regions correspond to structures that show unique morphology. For instance, Regimes 1, 2, 3 and 4 represents positive index modified structures, uniform negative index modified structures (such as voids), fragmented negative (soft) index modified structures, and fragmented negative (strong) index modified structures, respectively.

A few important points should be made when BG beams interact with a condensed transparent medium such as glass, thereby resulting in a permanent material modification. First, BG beams are more robust to Kerr nonlinearities than Gaussian beams. For instance, it has been shown that the "self-focusing effects" that play a decisive role (obstructive) in energy deposition inside the medium (which dictates the type of material modification) can be substantially suppressed using high cone angle BG beams, and over a wide variety of energetic conditions, primarily due to the conical nature of the energy flow. In contrast, control of high-energy Gaussian beams is very challenging. Second, when femtosecond and picosecond BG beam are compared, the latter is more stable in the presence of nonlinearity of the medium. This is mainly because the plasma defocusing effect is substantially suppressed due to delayed ionization mechanisms triggered by the picosecond laser beam. The leading part of the femtosecond laser pulse can swiftly generate free carriers in the medium, which have the potential to scatter the remainder of the pulse. However, generally speaking, a picosecond laser pulse of the same energy produces a smaller number of carriers at the leading edge of the pulse due to its low peak intensity (in comparison to a femtosecond pulse), so a low carrier scattering effect can be observed. Additionally, the avalanche effect is more pronounced in the case of picosecond BG beams, which
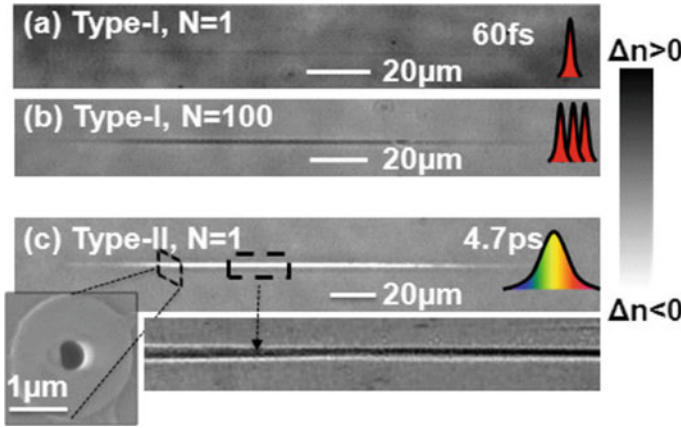
Fig. 6.14 Phase contrast microscopy (PCM) images of BG beam ($\theta = 8.3°$) induced high aspect ratio structures at two different pulse durations. **a** Single pulse based Type-I positive refractive index structure machined using 1.7 μJ pulse energy and 60 fs. **b** Multiple pulse (pulse number, N = 100) based smooth Type-I refractive index structure machined using 1 μJ, 60 fs. **c** Single pulse based Type-II uniform void structure machined using 7 μJ, 4.7 ps. Typical SEM cross-sectional profiles for the fabricated structures at picosecond pulse durations demonstrating submicron lateral confinement are also shown (inset) [133]. Reproduced with permission from Wiley
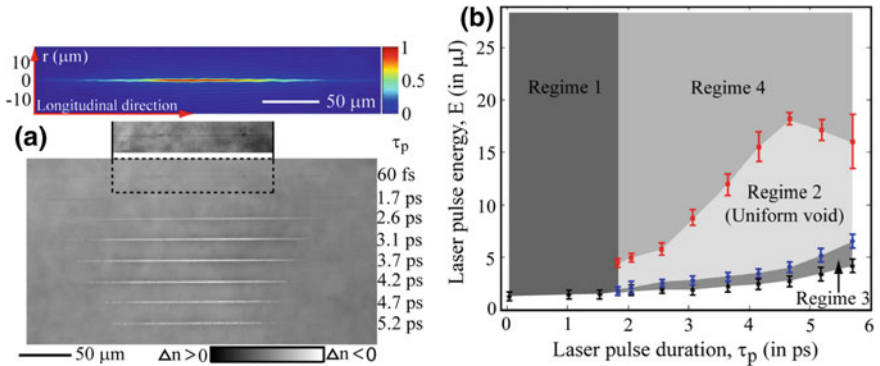

Fig. 6.15 BG beam based bulk structuring results: **a** Pulse duration dependent morphological characteristics of single pulse induced long structures in fused silica glass, showing the gradual evolution from positive to negative refractive index changed structures, **b** energetic conditions in the framework of pulse energy and temporal duration for the machining of structures with different morphologies [132]. Reproduced with permission from AIP

ultimately boosts the carrier number density. This is the reason why, compared with their femtosecond counterparts, picosecond laser pulses are generally more efficient in terms of energy deposition inside a medium.

Indeed, through numerical simulation studies, Bhuyan et al. [132] demonstrated that energy deposition approximately an order of magnitude higher can be obtained

inside glass when it is excited by a picosecond (such as 4.7 ps) BG beam with a conical half-angle of 8.3° and a pulse energy of 4.1 μJ, instead of a femtosecond (such as 60 fs) BG beam. Nevertheless, these results pertaining to the nonlinear Bessel beam propagation dynamics in glass indicate the achievement of a high deposited energy density (a few kJ/cm^3, sufficient to trigger a phase change of material) only in the picosecond case. As an extreme case, the temporal engineering concept was applied to a loose focusing geometry, and remarkably long voids with lengths of up to 1 mm and diameters of down to 100 nm were obtained on single-pulse basis, using zero-order BG beams with a conical half-angle of 4.2° (in glass), 1 ps pulse duration, and an energy of just a few microjoules [133].

In brief, void-like structures with potential applications in the field of photonics and fluidics can be realized using BG beams of low and moderate conical half-angles ($\theta <$ nearly 10°) only when a temporal engineering concept (that produces ps pulses) is employed. However, Bhuyan et al. [121] were the first to demonstrate that a single femtosecond BG laser pulse in a tight focusing geometry can drastically alter the material properties, and thus produce voids inside transparent materials. This technique has been explored for different transparent materials such as borosilicate glass [121, 134], fused silica glass [132], sapphire [135], polymers [135–138] and others. Figure 6.16a shows an SEM cross-sectional image of a 21 μm long and 300 nm diameter nanochannel in borosilicate glass that was machined using a single femtosecond BG pulse ($\theta = 17°$ in glass) of 0.85 μJ energy. The channel characteristics have also been observed to be scalable [121]. For instance, the region of the material over which the BG central core intensity exceeds approximately 10^{12-13} W/cm^2 [2] primarily dictates the channel length. This implies that higher is the pulse energy, longer is the channel length, until reaching a saturation value. In contrast, the channel diameter estimation is difficult as the underlying mechanism (which is still being debated) is not yet fully understood. Nevertheless, Bhuyan et al. [121] experimentally obtained a near-linear scaling of channel diameter with respect to the laser pulse energy. One of the important features of single-pulse BG beam machining is that by keeping the pulse energy fixed, the channel length can be varied straightforwardly, without affecting the channel diameter, simply by suitably placing the BG beam within the medium. Note that this unique feature of de-coupling channel length-diameter is not possible with Gaussian beam machining due to its complex and unpredictable beam propagation dynamics.

From a technological viewpoint, BG beam induced extended nanochannels are suitable for numerous applications. For instance, the deep drilling (up to a millimeter) capability of BG beams is unique and far exceeds other state-of-the-art techniques [74–77]. Bhuyan et al. [132] demonstrated water flow through BG beam induced nanochannels in fused silica glass, thereby opening novel possibilities for designing nanoscale devices, such as by injecting suitable nanoparticles inside channels. With an aim towards replicating the design of a photonic crystal, Bhuyan et al. [121] demonstrated a 2D nanochannel array comprised of machined channels (230 nm in diameter and a few tens of microns long), as shown in Fig. 6.16b. The other application that BG beam machining technology aims at is high throughput slicing and/or cutting of thick transparent materials. The methodology of such cutting technique is
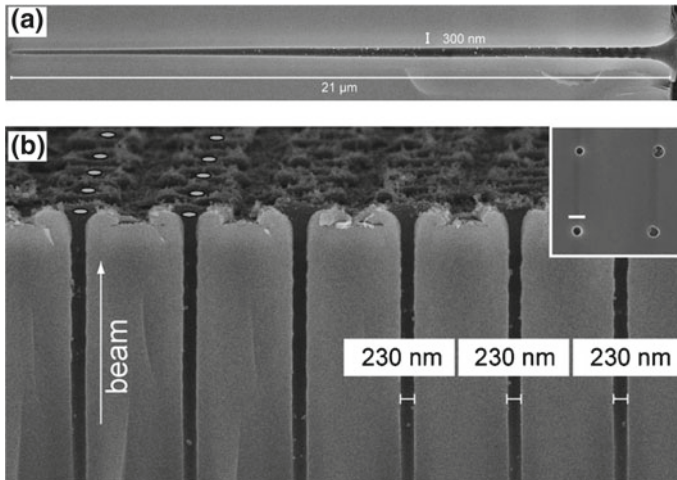
Fig. 6.16 BG beam ($\theta = 17°$) based nanostructuring results. **a** SEM cross-sectional image of a typical nanochannel produced in Corning 0211 glass using a single Bessel pulse of 0.85 µJ energy, and **b** SEM cross-sectional image of a nanochannel array obtained using almost the same machining conditions [121]. Reproduced with permission from AIP

as follows: (a) Choose the laser energy needed to machine a uniform channel-like structure (although strong non-uniform material modification can be used if compromised with the cut surface quality) inside the material using a single laser pulse. Although the length of the channel is not especially critical, the best cutting results are obtained in cases where the channels extend over the sample thickness (especially for inhomogeneous materials such as tempered glass [139]). (b) Optimize the distance between consecutive channels (pitch), which depends on the channel morphology and the lateral dimensions. The pitch values used for cutting experiments thus far are reported to lie between 0.5 and 10 µm. (c) Select the effective number of laser pulses per spot. Ideally, the best case would be achieved using a single laser pulse per spot. However, if single pulse induced material modification is not sufficiently strong, multiple laser pulses per spot will be required. (d) Apply mechanical pressure on either side of the plane containing channel-like structures to achieve cutting of the material.

Several research efforts [138–141] have been made in this direction. For instance, Tsai et al. [140] first exploited femtosecond (120 fs) zero-order BG beams (2 µm core diameter) to realize cutting of 100 µm thick fused silica glass (homogeneous along the sample thickness) at a speed of 1 µm/s (laser repetition rate of 1 kHz, and a pitch of 1 µm), whereas Bhuyan et al. [139] demonstrated cutting of homogenous glass and inhomogeneous tempered glass with thicknesses of up to 1 mm, at a speed up to 270 mm/s (laser repetition rate of 60 kHz), using picosecond BG beams with 2.5 µm core diameter. Those authors also reported that pitch is an important factor for high-quality cutting, as shown in Fig. 6.17a. For instance, an optimum pitch of
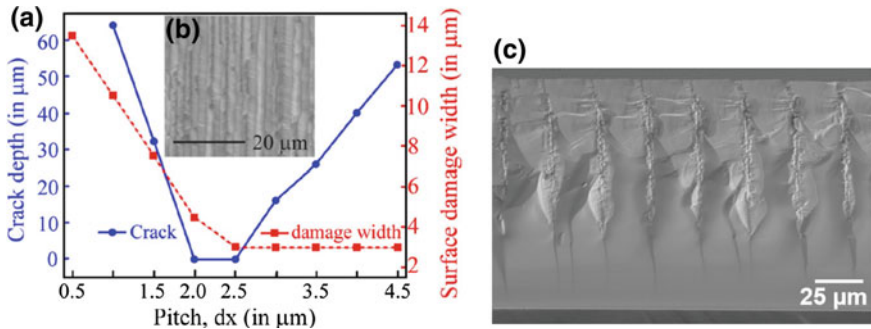
Fig. 6.17 Experimental results of BG beam-based cutting of transparent materials. **a** Sample crack evaluation with respect to the pitch, i.e., distance between consecutive BG beam induced material modifications inside a 700 μm thick tempered glass, **b** typical cut surface of a tempered glass [139]. **c** SEM cross-sectional image of a cut surface of sapphire sample machined with a pitch of 25 μm [141]. Reproduced with permission from Springer and OSA

2 ± 0.5 μm was observed for sample cleaving with minimum surface damage. Rapp et al. [141] also demonstrated sapphire plate cutting using a zero-order BG beam with an exceptionally high pitch (25 μm), as illustrated in Fig. 6.17c. The possibility of cutting with a large pitch was facilitated by preferential crack propagation along the crystal orientation axis. In short, the deep drilling capability of BG beams can be highly beneficial for high-speed cutting of thick materials, irrespective of sample homogeneity along the sample thickness direction.

To better understand and control material processing using BG beams, it is necessary to study the dynamics of material modification. First, since it was clarified that nanoscale yet extended material modifications could be obtained either completely inside the material or with a structure opening on the sample surfaces, the question of whether the dynamics of material modification in each separate case are the same requires consideration. Second, since various structural modification types, such as positive and negative refractive index changes, can be obtained using BG beams with the same focusing geometry and the same pulse energy, but different pulse durations, this again opens up the question of whether the dynamics of both structure types are the same, or if they follow the same route. Although the exact mechanism is yet to be clarified, a number of mechanisms have been proposed based on the experimental findings obtained thus far. The ultrafast dynamics of extended structures machined in glass using zero-order BG beams were first revealed by Velpula et al. [133, 142] using time-resolved optical microscopy techniques. In these experiments, the optical transmission mode was employed to study the behavior of laser induced plasmas, i.e., free carriers inside glass through their scattering and/or absorption natures. PCM mode was employed to track the relative phase change of the excited matrix. The carrier density was then estimated from the absorption characteristics of the excited regions at a fixed time delay with respect to the laser excitation, based on the Drude model [6, 133, 142]. Ideally, laser-excited matter dynamics would be independent of
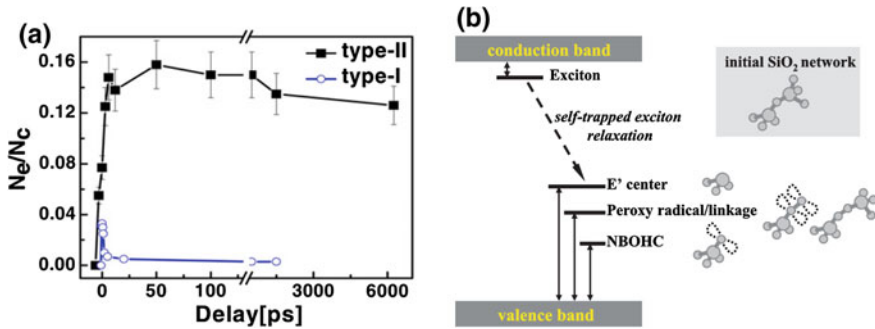
Fig. 6.18 Ultrafast dynamics of fused silica glass excited by BG beams: **a** variation of peak carrier density with respect to the delay time in cases of material modification with both increased (Type-I) and decreased (Type-II) refractive indices [133], **b** schematic illustration of exciton and intrinsic defect energy levels in SiO$_2$ [6]. Reproduced with permission from Wiley and Springer

the spatial profiles (such as Gaussian, Bessel) of the incident laser beam. However, given the advantage of extended scale matter excitation, which makes the visualization of transient features clearer, the study of matter excited with BG beams is more appealing.

The carrier dynamics corresponding to increased (Type-I) and decreased (Type-II) refractive index structures machined using 8.3° BG beams in fused silica glass, as shown in Fig. 6.18a, are observed to be different from each other. For the Type-I structure, which can be obtained primarily using a single femtosecond BG pulse, the carrier number density swiftly increases, reaching a maximum value that is about an order of magnitude less than the critical value in vacuum ($N_{cr} = 1.74 \times 10^{21}$/cm^3 for 800 nm light), and decreases to almost zero within a few picoseconds after laser excitation. This behavior is often associated with carrier trapping (lifetime of 150 fs in SiO$_2$ matrix [6]).

The carriers trapped in their own deformed matrix then result in self-trapped exciton formation. Such excitons are very transient (see Fig. 6.18b), and upon relaxation decay into electronic defects known as E$'$ centers and non-bridging oxygen-hole center (NBOHC). Earlier reports on Gaussian beam excited glass dynamics have revealed that NBOHC defects form smaller Si-O rings, and hence create a compact matrix. Therefore, increased refractive index structures are believed to be formed via electronic defects. In contrast, for the Type-II structure, which can be obtained primarily using a single picosecond BG pulse, the carrier number density increased to a near-critical value and remained almost constant until 17.5 ns, without showing any observable carrier trapping signature. Earlier reports [132, 133] have clarified, through numerical simulations, that the temperature rise in this case can indeed be close to (or above) the fused silica matrix softening point, which is about 1000 °C. Therefore, at such high temperatures, carrier trapping is not expected. For these machining conditions, the pressure waves [133, 143] can be visualized following 1 ns of laser excitation, thereby indicating the existence of high-level matter

excitation, which can lead to a high temperature and pressure state. As a result, a micro-explosion may occur over the excited zone, compressing the material along the outward direction and leaving behind a rarified zone at the excitation epicenter. The existence of a high temperature and pressure state was also argued based on the fact that molten material can be obtained at the exit opening of such Type II structures (channels/voids) when they are machined in an appropriate way (see inset to Fig. 6.14c). It was then argued that the hot excited matter must have been ejected from the bulk and deposited around the channel. Therefore, the decreased refractive index structures are believed to be formed due to the high temperature and pressure driven thermo-mechanical expansion of glass. Very recently, Bhuyan et al. [144] reported that the timescale of emergence of such void-like structures (resulting from stress relaxation) can be up to a few hundred nanoseconds, which is otherwise believed to be on the ultrafast timescale [7]. However, more advanced imaging and microscopy tools will be required in order to examine the unique light-matter interaction processes involving non-diffracting zero-order BG beams.

6.4.2 Vortex Beams

Optical vortex beams with zero intensity at the center, and concentric high intensity lobes, have attracted significant attention in fields such as nonlinear optics and plasma physics [102, 144–151], optical tweezers [105, 152], and material processing [151, 152–157]. Femtosecond optical vortices have been generated using spiral phase plates [157–161], holograms [151, 155], and uniaxial birefringent crystals [153, 162]. Interestingly, however, when such high-intensity femtosecond vortex beams are employed for surface processing, an unusual light-matter interaction geometry is facilitated, resulting in the creation of a dense plasma zone in a toroidal region of the material. As a result, ablation within the ring (down to micrometer size) may occur even when using a single laser pulse. Hnatovsky et al. [153] first exploited such a concept and machined highly reproducible microstructures on glass, as shown in Fig. 6.19a, b. One of the more striking observations from that figure is that, upon increasing the laser pulse energy, deep cavities started to form at the center of the annulus ring-type structure. This was attributed to shock wave (moving towards the ring center) driven material compression and ejection. This technique can be potentially useful for the direct fabrication of isolated nanoparticles of different materials.

   Non-diffractive higher-order Bessel beams (J_m), consisting of concentric cylindrical regions with gradual diminishing intensity from the inner to outer regions, and Laguerre-Gaussian beams, are also representative of the vortex beam class, and have been exploited for material processing. Like zero-order Bessel beams, ideal higher-order Bessel beams also require infinite levels of energy. However, finite-energy versions of such higher-order Bessel beams can be realized using Gaussian beams passing through a spiral phase plate followed by an axicon lens, or a spatial light modulator masked with a suitable phase. In any case, the vortex charge or helicity (integer values) determines the size of the intense inner ring of the corresponding
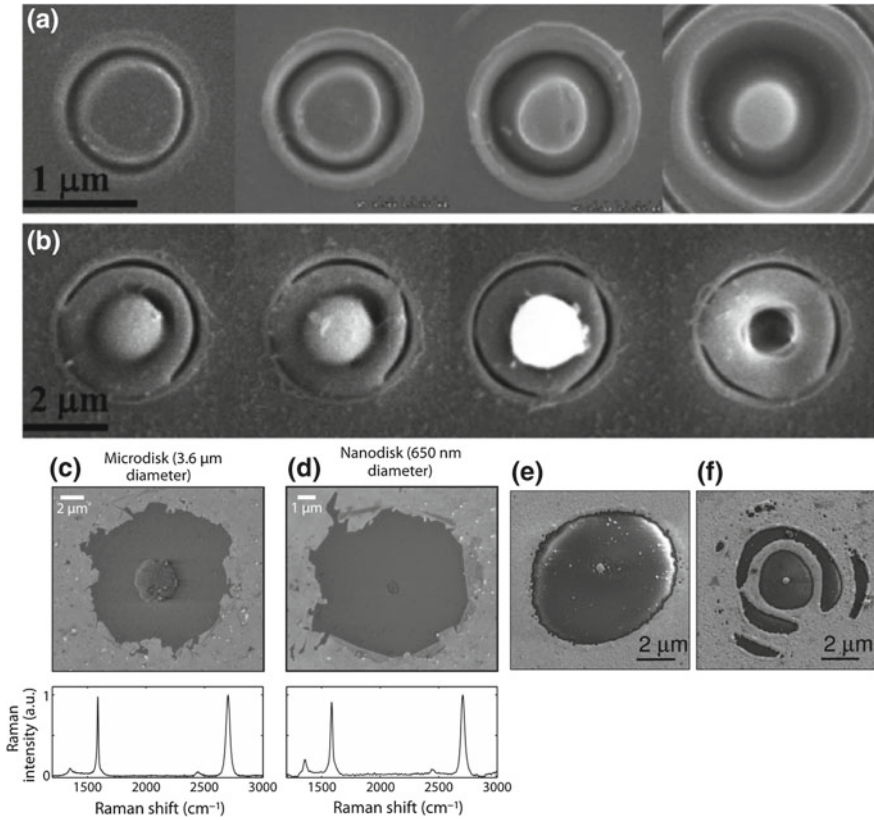
Fig. 6.19 Vortex beam-based surface structuring results: **a**, **b** single pulse ablation of soda-lime glass with double-charge femtosecond vortex pulses using a focusing lens of 0.9 NA [153], **c**, **d** micro- and nano-disks machined on graphene using higher-order Bessel beams in multi-pulse exposure scheme [154], **e**, **f** nano-disks machined on gold film using femtosecond laser first-order Bessel beams [156]. Reproduced with permission of OSA and AIP

Bessel beam. This opens up the novel possibility of designing a light-matter interaction geometry in the form of a cylinder with an arbitrary radius. For instance, using femtosecond laser vortex beams, Wetzel et al. [154] fabricated micro- and nano-disks with sizes as small as 650 nm on some of the most technologically demanding materials available, such as graphene, with clear boundaries confirmed via Raman spectroscopy (see Fig. 6.19c, d). Similarly, Sahin et al. [156] fabricated nano-disks as small as 200 nm on a gold thin film using a femtosecond first-order Bessel beam, as shown in Fig. 6.19e. They also pointed out that concentric rings formed around the central intense ring may produce unwanted structures for higher laser fluences (see Fig. 6.19f).

Vortex beams such as higher-order Bessel beams with an extended depth of focus have also been demonstrated for volume fabrication (i.e., internal material modi-

fication) [151, 157]. The underlying process in such cases is almost the same as that for a zero-order Bessel beam. For instance, the nonlinear propagation stability (in the presence of nonlinearity of the medium and multiphoton loss) of first-order Bessel beams [147–150] in a Kerr medium such as glass, is obviously an important factor for uniform energy deposition inside the medium. This is mainly because the multiphoton absorption loss in the high-intensity regions (innermost cylinder) is readily compensated for by the inward energy flow associated with the conical nature of first-order Bessel beams. Similar to the case for zero-order Bessel beams, several researchers [149, 150] have discovered parametric windows that provide stability criteria for nonlinear first-order Bessel beams. Apart from parameters such as the laser pulse energy and the pulse duration, the stability of Bessel beams is extremely sensitive to the cone angle. In other words, higher is the cone angle, better is the nonlinear stability of Bessel beams. For instance, since self-phase modulation and four-wave mixing effects modify the spatial spectrum, modulations to the axial intensity distribution (primarily on the inner cylinder of first-order Bessel beams) are very dominant in the case of low cone angle Bessel beams. Generally speaking, axial intensity modulation results in non-uniformity of the processed structure. In addition, the maximum intensity, and hence the plasma density in the cylindrical (innermost) region of higher order Bessel beams, can be obtained with a lower vortex charge value (smaller inner cylinder diameter).

Therefore, for material processing applications, an optimum balance between the vortex charge and the cone angle for higher-order Bessel beams is highly important, depending on the material to be processed and the type of structure to be obtained. For instance, Bessel beams that have cone angles (in glass) larger than $5°$ can trigger peak electron densities of more than 10^{19} cm^{-3}, thus facilitating sufficient energy deposition to induce a permanent material modification, as shown in Fig. 6.20a [151]. Xie et al. [151] first exploited vortex Bessel beams (higher order) for volume fabrication of Corning glass and obtained a tube-like refractive index modified structure for potential waveguide applications, as illustrated in Fig. 6.20b. A single pulse (35 μJ energy and 1 ps temporal duration) was shown to be capable of machining a 150 μm long cylindrical positive index modified zone with a 5 μm diameter using J_3 vortex beams. The refractive index change was estimated to be around 10^{-4} from the light (633 nm) guiding experiments (see Fig. 6.20d for the guided mode profile). Figure 6.20e schematically shows the directions of inwardly and outwardly propagating cylindrical matter waves generated by the tubular plasma. These are shock, pressure, and heat waves. Jedrkiewcz et al. [157] demonstrated cylindrical refractive index modifications (wall thickness and diameter of approximately 1 and 8 μm, respectively) in 100 μm thick BK7 glass using a J_8 vortex beam (37 μJ pulse energy, 1 ps temporal duration) with a conical half-angle of $11°$ (in the medium). Note that a hollow structure fabricated by a single vortex pulse can also be fabricated using a hollow Gaussian beam in a multi-pulse illumination regime with continuous sample translation. However, vortex beams clearly show superiority in terms of fabrication speed and structural uniformity.
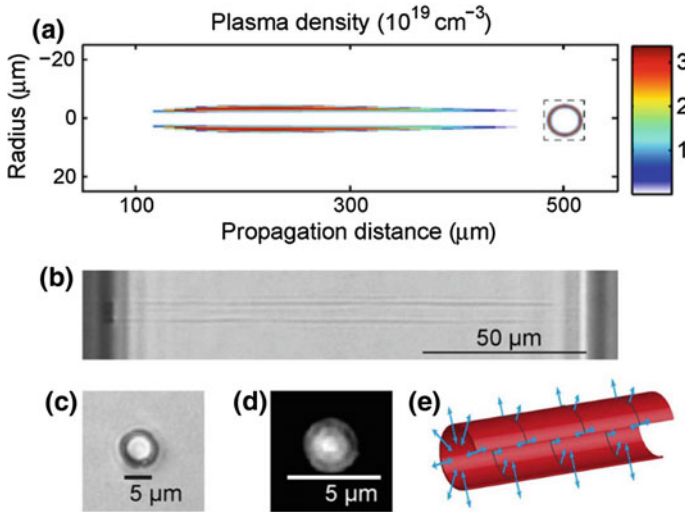
Fig. 6.20 Vortex beam (J_3 beam, $\theta = 6.8°$) based micro-structuring results. **a** Electron density distribution inside 150 μm thick glass excited with 5 μJ pulse energy, obtained by numerical simulations. **b** Optical micrograph (longitudinal view) of a typical tubular structure machined (35 μJ pulse energy, 1 ps pulse duration) in glass on single-shot basis. **c** Transverse section of the damage observed under identical machining conditions, but using 20 μJ pulse energy. **d** Image of near-field output guided light in the structure shown in (**c**), at an input wavelength of 632 nm. **e** Schematic view of the propagation direction of mechanical and thermal waves expanding outward and inward (arrows) from the excited tubular sheet volume (circle) [151]. Reproduced with permission from NPG

6.4.3 Curved Beams

An ideal Airy beam, discovered by Berry et al. [90], is basically a solution of the paraxial wave propagation equation, which is non-diffractive in nature. Similar to zero-order Bessel beams, such beams also possess a central intense spot, and propagate over an infinite distance with no diffraction, and uniquely along a parabolic (i.e., curved) trajectory. Like other non-diffractive beams, Airy beams also exhibit self-reconstruction characteristics [94]. Notably, Airy beams require an infinite level of energy in order to manifest their diffraction-free propagation characteristics in free space. Siviloglou et al. [91] first derived a finite energy Airy beam solution by modulating an ideal Airy beam with an exponential decay function. In this case, the field in the $\zeta = 0$ plane is assumed to have form of $\psi(s, \zeta = 0) = \text{Ai}(s) \exp(as)$, where Ai denotes the Airy function, and a is a real positive constant. $s = x/x_0$ and $\zeta = z/kx_0^2$ are the dimensionless transverse and longitudinal coordinates respectively, x_0 is the spatial spot size and $k = 2\pi/\lambda_0$ is the wavenumber of the optical wave. Upon substituting this initial field ($\zeta = 0$ plane) profile in the 2D paraxial envelope equation ($i\partial\zeta\psi + 1/2\partial^2 s\psi = 0$), one can obtain the generalized Airy-Exponential field solution as follows:
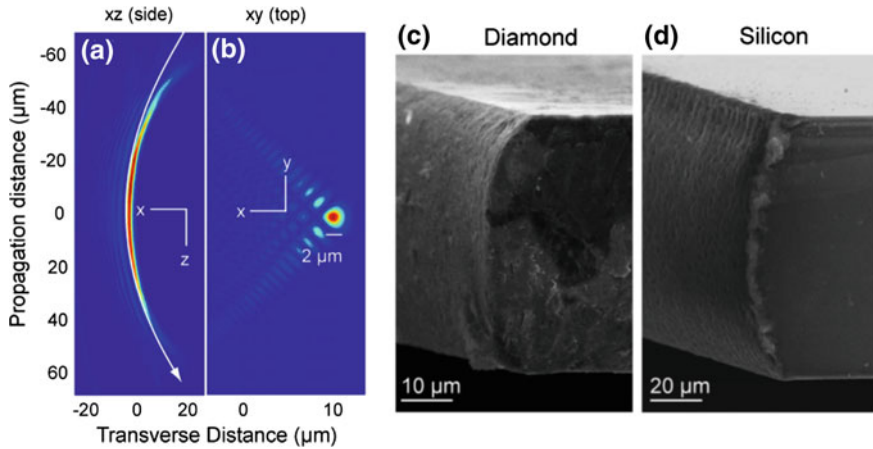
Fig. 6.21 Airy beam-based cutting results: Longitudinal (**a**) and transverse (**b**) cross-sectional images of a typical airy beam generated using a spatial light modulator. Cross-sectional SEM images of cut surfaces of (**c**) diamond and (**d**) Si [170]. Reproduced with permission from AIP

$$\psi(s, \zeta) = \text{Ai}\left[s - (\zeta/2)^2 + ia\zeta\right] \exp\left[as - \left(a\zeta^2/2\right) - i\left(\zeta^3/12\right) + i\left(a^2\zeta/2\right) + i(s\zeta/2)\right].$$

From an experimental viewpoint, finite energy (usually by beam apodization) Airy beams can be generated using a phase mask [100, 163, 164], SLM [164–167], or an optically induced refractive index gradient [168]. Airy beams with central lobe sizes down to the sub-micron scale, which are useful in many important applications, have been generated [99, 100, 106, 108, 169]. These applications include flexible material processing [165, 170, 171], where the existence of stable nonlinear Airy beams is beneficial [172, 173]. Note here that the size (d_a, FWHM) of the central lobe of the Airy beams can be related to the curvature radius over which the beam bends, as $d_a = 1.63 \, [R/2k^2]^{1/3}$, where R is the trajectory curvature radius [166]. This implies that the higher the curvature radius, the lower the Airy central lobe size. Figure 6.21a, b show typical longitudinal and transverse cross-sectional images of experimentally generated (via SLM) Airy beams with an arc-shaped (curvature radius of 120 µm) central lobe size of 2 µm extended longitudinally over several tens of microns, as reported by Mathis et al. [170].

When such a beam is used for bulk structuring of materials, the intense curved central lobe is expected to ablate and/or modify the material in a way similar to Bessel beams, but along a curved line if operating in the above-ablation threshold regime. This unique curved machining feature of Airy beams has been exploited for cutting or dicing of technologically important materials such as diamond and Si by following the same methodology used for Bessel beams and filamentation based cutting [36, 139, 140]. For instance, using a pulsed laser source with 800 nm wavelength, 100 fs pulse duration, and 11 µJ pulse energy, Mathis et al. [170] demonstrated cutting (laser material modification followed by cleaving) of 50 µm thick diamond slides

with cut surface circular profile radius of 70 µm by suitably machining individual curved structures (pitch of 0.3 µm) along a certain direction, as shown in Fig. 6.21c. Using parameters similar to those described above, except with a pitch of 0.5 µm, the same authors also demonstrated cutting 100 µm thick Si (see Fig. 6.21d for a cross-sectional SEM image of the cut surface) with cut surface circular profile radius of 120 µm. Note that the above cutting demonstrations were realized using a two-pass configuration (effectively, two laser pulses at each spot). Airy beams thus provide an additional degree of control along with mechanical sample rotation or beam steering that can be used to obtain round-cornered, thick materials with curved surface profiles. Besides cutting, curved trench machining using Airy beams was also demonstrated by the same authors [171]. One of the striking observations that they made was the asymmetric debris distribution (present only one side of trench) around the trench, which can be of technological importance in situations where sample cleaning is critical after processing. This unique debris distribution was attributed to the asymmetric intensity profile, as shown in Fig. 6.21a, b.

6.5 Conclusions

In the 30 years since the first ultrafast laser processing experiments were demonstrated by Srinivasan et al. [174] and Küper et al. [175] in 1987, research into this field has become increasingly more active. This is because, due to distinct features such as ultrashort pulse width and extremely high peak intensity, ultrafast lasers offer novel schemes for processing materials that are not accessible using other types of lasers. In particular, the clean ablation ability of ultrafast lasers and their associated multiphoton absorption processes surprised numerous researchers, and opened a new door for high-quality processing of transparent materials [176]. Breakthroughs in terms of internal modification or volume fabrication of transparent materials, such as glass, further accelerated the growth of this field [10, 11, 23]. It was also demonstrated that the multiphoton absorption processes in the near-threshold ablation regime can even lead to fabrication resolution down to a few tens of nanometers, which is far beyond the diffraction limit [13, 14]. Therefore, material fabrication at micro and nanoscale levels is currently one of the major activities in the field of ultrafast laser processing, and has numerous potential applications in the fields of electronics, healthcare, photonics, and energy harvesting. One of the most successful commercial applications of the ultrafast laser processing of transparent materials is scribing and dicing very thin and hard glass in order to produce high-quality edges, flexible geometry, and crack-free components for use in the mass production of displays for cell phones and tablet computers. Meanwhile, from the viewpoint of recent fundamental research, attention is being focused on nanoprocessing based on the nonlinear light confinement processes in order to produce structures of lateral sizes down to few nanometers. Near-field optical phenomena can also be used to improve the fabrication resolution. Further challenges lie in facilitating the deep machining of transparent materials while maintaining micro and nanoscale lateral sizes (high aspect ratio machining).

Non-diffractive optical beams represented by zero-order Bessel beams possessing a long (along the longitudinal direction), narrow and intense region, have become promising tools for high aspect ratio material processing. For example, voids with lengths up to a millimeter and diameters down to 100 nm have been fabricated inside fused silica glass on a single-pulse basis using temporally engineered zero-order Bessel beams [133]. Other non-diffractive optical beams, such as vortex and Airy beams, enable us to imprint new types of structures that cannot be achieved by other techniques. For example, the former can produce tube-like structures, while the latter can produce longitudinally curved structures.

Ultrafast laser processing is already used for commercial and industrial applications, and this trend is expected to be further accelerated because of the distinct advantages ultrafast laser processing has over conventional laser processing or other existing competing techniques. To this end, current research activities are not only focusing on developing advanced processing techniques, but are also aimed at elucidating the detailed mechanisms of ultrafast laser-matter interactions. It is now believed that spatiotemporal beam shaping, including the generation of non-diffractive optical beams, will be one of the key technologies driving future improvements to the fabrication resolution, quality, and efficiency of ultrafast laser based manufacturing.

References

1. S. Nolte, G. Kamlage, F. Korte, T. Bauer, T. Wagner, A. Ostendorf, C. Fallnich, H. Welling, Adv. Eng. Mat. **2**, 23 (2000)
2. R.R. Gattass, E. Mazur, Nat. Photonics **2**, 219 (2008)
3. G.D. Valle, R. Osellame, P. Laporta, J. Opt. A: Pure Appl. Opt. **11**, 013001 (2008)
4. K. Sugioka, Y. Cheng, Light: Sci. Appl. **3**, e149 (2014)
5. Y. Shimotsuma, P.G. Kazansky, J. Qiu, K. Hirao, Phys. Rev. Lett. **91**, 247405 (2003)
6. S. Mao, F. Quéré, S. Guizard, X. Mao, R. Russo, G. Petite, P. Martin, Appl. Phys. A **79**, 1695 (2004)
7. S. Juodkazis, K. Nishimura, S. Tanaka, H. Misawa, E.G. Gamaly, B. Luther-Davies, L. Hallo, P. Nicolai, V.T. Tikhonchuk, Phys. Rev. Lett. **96**, 166101 (2006)
8. A. Mermillod Blondin, J. Bonse, A. Rosenfeld, I.V. Hertel, YuP Meshcheryakov, N.M. Bulgakova, E. Audouard, R. Stoian, Appl. Phys. Lett. **94**, 041911 (2009)
9. D. Du, X. Liu, G. Korn, J. Squier, G. Mourou, Appl. Phys. Lett. **64**, 3071 (1994)
10. K.M. Davis, K. Miura, N. Sugimoto, K. Hirao, Opt. Lett. **21**, 1729 (1996)
11. E.N. Glezer, E. Mazur, Appl. Phys. Lett. **71**, 882 (1997)
12. H. Helvajian, *Direct-Write Technologies for Rapid Prototyping Applications*, ed. by A. Piqué, D.B. Chrisey (Academic Press, San Diego, CA, 2002), Chapter 14
13. A.P. Joglekar, H. Liu, G.J. Spooner, E. Meyhofer, G. Mourou, A.J. Hunt, Appl. Phys. B Lasers Opt. **77**, 25 (2003)
14. A.P. Joglekar, H. Liu, E. Meyhofer, G. Mourou, A.J. Hunt, PNAS **101**, 5856 (2004)
15. J.F. Herbstman, A.J. Hunt, Opt. Express **18**, 16840 (2010)
16. A. Rosenfeld, M. Lorenz, R. Stoian, D. Ashkenasi, Appl. Phys. A **69**, S373 (1999)
17. D. Ashkenasi, M. Lorenz, R. Stoian, A. Rosenfeld, Appl. Surf. Sci. **150**, 101 (1999)
18. C.B. Schaffer, J.F. Garcia, E. Mazur, Appl. Phys. A **76**, 351 (2003)
19. R. Osellame, N. Chiodo, G. Della Valle, S. Taccheo, R. Ramponi, G. Cerullo, Opt. Lett. **29**, 1900 (2004)

20. S.M. Eaton, H. Zhang, P.R. Herman, F. Yoshino, L. Shah, J. Bovatsek, A.Y. Arai, Opt. Express **13**, 4708 (2005)

21. M. Shimizu, M. Sakakura, M. Ohnishi, Y. Shimotsuma, T. Nakaya, K. Miura, K. Hirao, J. Appl. Phys. **108**, 073533 (2010)

22. C. Kerse, H. Kalaycioglu, P. Elahi, B. Cetin, D.K. Kesim, O. Akcaalan, S. Yavas, M.D. Asik, B. Oktem, H. Hoogland, R. Holzwarth, F.O. Ilday, Nature **537**, 84 (2016)

23. E.N. Glezer, M. Milosavljevic, L. Huang, R.J. Finlay, T.-H. Her, J.P. Callan, E. Mazur, Opt. Lett. **21**, 2023 (1996)

24. G.D. Marshall, A. Politi, J.C.F. Matthews, P. Dekker, M. Ams, M.J. Withford, J.L. O'Brien, Opt. Express **17**, 12546 (2009)

25. T. Meany, Laser Focus World **50**, 25 (2014).

26. Y. Nasu, M. Kohtoku, Y. Hibino, Opt. Lett. **30**, 723 (2005)

27. J. Lapointe, Y. Ledemi, S. Loranger, V.L. Iezzi, E.S.L. Filho, F. Parent, S. Morency, Y. Messaddeq, R. Kashyap, Opt. Lett. **41**, 203 (2016)

28. J. Guan, X. Liu, P.S. Salter, M.J. Booth, Opt. Express **25**, 4845 (2017)

29. W. Watanabe, T. Asano, K. Yamada, K. Itoh, J. Nishii, Opt. Lett. **28**, 2491 (2003)

30. C. Florea, K.A. Winick, J. Lightwave Technol. **21**, 246 (2003)

31. L. Sudrie, M. Franco, B. Prade, A. Mysyrowicz, Opt. Commun. **191**, 333 (2001)

32. E. Bricchi, J.D. Mills, P.G. Kazansky, B.G. Klappauf, J.J. Baumberg, Opt. Lett. **27**, 2200 (2002)

33. G.D. Valle, S. Taccheo, R. Osellame, A. Festa, G. Cerullo, P. Laporta, Opt. Express **15**, 3190 (2007)

34. L. Sudrie, A. Couairon, M. Franco, B. Lamouroux, B. Prade, S. Tzortzakis, A. Mysyrowicz, Phys. Rev. Lett. **89**, 4135 (2002)

35. A. Couairon, A. Mysyrowicz, Phys. Rep. **441**, 47 (2007)

36. C.-H. Tsai, C.-S. Liou, J. Manuf. Sci. Eng. **125**, 519 (2003)

37. F. Ahmed, M. Lee, H. Sekita, T. Sumiyoshi, M. Kamata, Appl. Phys. A **93**, 189 (2008)

38. S. Nisar, L. Li, M.A. Sheikh, J. Laser Appl. **25**, 042010 (2013)

39. S. Butkus, D. Paipulas, R. Sirutkaitis, E. Gaizauskas, V. Sirutkaitis, J. Laser Micro/Nano Eng. **9**, 213 (2014)

40. K. Mishchik, C.J. Leger, O.D. Caulier, S. Skupin, B. Chimier, C. Honninger, R. Kling, G. Duchateau, J. Lopez, J. Laser Micro/Nano Eng. **11**, 66 (2016)

41. J. Schwarz, J.-C. Diels, Appl. Phys. A **77**, 185 (2003)

42. D.G. Papazoglou, I. Zergioti, S. Tzortzakis, Opt. Lett. **32**, 2055 (2007)

43. L. Shah, J. Tawney, M. Richardson, K. Richardson, Appl. Surf. Sci. **183**, 151 (2001)

44. H. Varel, D. Ashkenasi, A. Rosenfeld, M. Wahmer, E.E.B. Campbell, Appl. Phys. A **65**, 367 (1997)

45. S.I. Kudryashov, G. Mourou, A. Joglekar, J.F. Herbstman, A.J. Hunt, Appl. Phys. Lett. **91**, 141111 (2007)

46. Y.V. White, X. Li, Z. Sikorski, L.M. Davis, W. Hofmeister, Opt. Express **16**, 14411 (2008)

47. S. Kanehira, J. Si, J. Qiu, K. Fujita, K. Hirao, Nano Lett. **5**, 1591 (2005)

48. H. Sun, J. Song, C. Li, J. Xu, X. Wang, Y. Cheng, Z. Xu, J. Qiu, T. Jia, Appl. Phys. A **88**, 285 (2007)

49. J. Song, X. Wan, X. Hu, Y. Dai, J. Qiu, Y. Cheng, Z. Xu, Appl. Phys. Lett. **92**, 092904 (2008)

50. H. Hu, H.J. Kim, S. Somnath, Micromachines **8**, 90 (2017)

51. A. Kirsanov, A. Kiselev, A. Stepanov, N. Polushkin, J. Appl. Phys. **94**, 6822 (2003)

52. D.J. Hwang, A. Chimmalgi, C.P. Grigoropoulos, J. Appl. Phys. **99**, 044905 (2006)

53. X. Li, Z. Chen, A. Taflove, V. Backman, Opt. Express **13**, 526 (2005)

54. A. Darafsheh, A. Fardad, N.M. Fried, A.N. Antoszyk, H.S. Ying, V.N. Astratov, Opt. Express **19**, 3440 (2011)

55. T.C. Hutchens, A. Darafsheh, A. Fardad, A.N. Antoszyk, H.S. Ying, V.N. Astratov, N.M. Fried, J. Biomed. Opt. **17**, 068004 (2012)

56. Y.F. Lu, L. Zhang, W.D. Song, Y.W. Zheng, B.S. Lukyanchuk, JETP Lett. **72**, 457 (2000)

57. H.-J. Munzer, M. Mosbacher, M. Bertsch, J. Zimmermann, P. Leiderer, J. Boneberg, J. Microsc. **202**, 129 (2001)
58. K. Piglmayer, R. Denk, D. Bauerle, Appl. Phys. Lett. **80**, 4693 (2002)
59. S.M. Huang, M.H. Hong, B.S. Lukyanchuk, T.C. Chong, Appl. Phys. A **77**, 293 (2003)
60. Y. Zhou, M.H. Hong, J.Y.H. Fuh, L. Lu, B.S. Lukyanchuk, Z.B. Wang, L.P. Shi, T.C. Chong, Appl. Phys. Lett. **88**, 023110 (2006)
61. S.C. Kong, A. Taflove, V. Backman, Opt. Express **17**, 3722 (2009)
62. Y. Shen, L.V. Wang, J.T. Shen, Opt. Lett. **39**, 4120 (2014)
63. C. Liu, Prog. Electromagn. Res. Lett. **37**, 153 (2013)
64. G. Gu, R. Zhou, Z. Chen, H. Xu, G. Cai, Z. Cai, M. Hong, Opt. Lett. **40**, 625 (2015)
65. Z. Hengyu, C. Zaichun, C.T. Chong, H. Minghui, Opt. Express **23**, 6626 (2015)
66. Y.E. Geints, A.A. Zemlyanov, E.K. Panina, J. Opt. Soc. Am. B **32**, 1570 (2015)
67. E. McLeod, C.B. Arnold, Nat. Nanotechnol. **3**, 413 (2008)
68. A. Ashkin, J.M. Dziedzic, J.E. Bjorkholm, S. Chu, Opt. Lett. **11**, 288 (1986)
69. V. Garces-Chavez, D. McGloin, H. Melville, W. Sibbett, K. Dholakia, Nature **419**, 145 (2002)
70. J. Durnin, J.J. Miceli, J.H. Eberly, Phys. Rev. Lett. **58**, 1499 (1987)
71. D. McGloin, K. Dholakia, Contemp. Phys. **46**, 15 (2005)
72. E. McLeod, A.B. Hopkins, C.B. Arnold, Opt. Lett. **31**, 3155 (2006)
73. S. Hasegawa, Y. Hayasaki, N. Nishida, Opt. Lett. **31**, 1705 (2006)
74. S. Hasegawa, H. Ito, H. Toyoda, Y. Hayasaki, Opt. Express **24**, 18513 (2016)
75. S. Juodkazis, L. Rosa, S. Bauerdick, L. Peto, R.E. Ganainy, S. John, Opt. Express **19**, 5802 (2011)
76. J. Gierak, Nanofabrication **1**, 35 (2014)
77. M.S. Alias, H.-Y. Liao, T.K. Ng, B.S. Ooi, J. Vac. Sci. Technol. B **33**, 06F701 (2015)
78. A.M. Weiner, Rev. Sci. Instrum. **71**, 1929 (2000)
79. D.J. Hwang, T.Y. Choi, C.P. Grigoropoulos, Appl. Phys. A **79**, 605 (2004)
80. Y. Li, K. Itoh, W. Watanabe, K. Yamada, D. Kuroda, J. Nishii, Y. Jiang, Opt. Lett. **26**, 1912 (2001)
81. Y. Iga, T. Ishizuka, W. Watanabe, K. Itoh, Y. Li, J. Nishii, Jpn. J. Appl. Phys. **43**, 4207 (2004)
82. K. Ke, E.F. Hasselbrink Jr., A.J. Hunt, Anal. Chem. **77**, 5083 (2005)
83. Y. Kondo, J. Qiu, T. Mitsuyu, K. Hirao, T. Yoko, Jpn. J. Appl. Phys. **38**, L1146 (1999)
84. S. Kiyama, S. Matsuo, S. Hashimoto, Y. Morihira, J. Phys. Chem. C **113**, 11560 (2009)
85. A. Marcinkevicius, S. Juodkazis, M. Watanabe, M. Miwa, S. Matsuo, H. Misawa, J. Nishii, Opt. Lett. **26**, 277 (2001)
86. Y. Cheng, K. Sugioka, K. Midorikawa, M. Masuda, K. Toyoda, M. Kawachi, K. Shihoyama, Opt. Lett. **28**, 55 (2003)
87. M. Masuda, K. Sugioka, Y. Cheng, N. Aoki, M. Kawachi, K. Shihoyama, K. Toyoda, H. Helvajian, K. Midorikawa, Appl. Phys. A **76**, 857 (2003)
88. K. Sugioka, Y. Cheng, K. Midorikawa, Appl. Phys. A **81**, 1 (2005)
89. K.C. Vishnubhatla, N. Bellini, R. Ramponi, G. Cerullo, R. Osellame, Opt. Express **17**, 8685 (2009)
90. M.V. Berry, Am. J. Phys. **47**, 264 (1979)
91. G.A. Siviloglou, D.N. Christodoulides, Opt. Lett. **32**, 979 (2007)
92. Y. Hu, G.A. Siviloglou, P. Zhang, N.K. Efremidis, D.N. Christodoulide, Z. Chen, *Nonlinear Photonics and Novel Optical Phenomena*. Springer series in optical sciences, vol. 170, ed. by Z. Chen, R. Morandotti (2012), p. 1
93. Z. Bouchal, J. Wagner, M. Chlup, Opt. Commun. **151**, 207 (1998)
94. J. Broky, G.A. Siviloglou, A. Dogariu, D.N. Christodoulides, Opt. Express **16**, 12880 (2008)
95. M.A. Porras, A. Parola, D. Faccio, A. Dubietis, P. Di Trapani, Phys. Rev. Lett. **93**, 153902 (2004)
96. D.E. Roskey, M. Kolesik, J.V. Moloney, E.M. Wright, Opt. Express **15**, 9893 (2007)
97. P. Polesana, M. Franco, A. Couairon, D. Faccio, P.D. Trapani, Phys. Rev. A **77**, 043814 (2008)
98. E. Gaizauskas, E. Vanagas, V. Jarutis, S. Juodkazis, V. Mizeikis, H. Misawa, Opt. Lett. **31**, 80 (2006)

99. I. Kaminer, M. Segev, D.N. Christodoulides, Phys. Rev. Lett. **106**, 213903 (2011)
100. P. Polynkin, M. Kolesik, J.V. Moloney, G.A. Siviloglou, D.N. Christodoulides, Science **324**, 229 (2009)
101. B. Hafizi, E. Esarey, P. Sprangle, Phys. Rev. E **55**, 3539 (1997)
102. J. Fan, E. Parra, I. Alexeev, K.Y. Kim, H.M. Milchberg, L.Y. Margolin, L.N. Pyatnitskii, Phys. Rev. E **62**, R7603 (2000)
103. M. Duocastella, C. Arnold, Laser Photonics Rev. **6**, 607 (2012)
104. F. Courvoisier, R. Stoian, A. Couairon, Opt. Laser Technol. **80**, 125 (2016)
105. V.G. Shvedov, A.V. Rode, Y.V. Izdebskaya, A.S. Desyatnikov, W. Krolikowski, Y.S. Kivshar, Phys. Rev. Lett. **105**, 118103 (2010)
106. J. Baumgartl, M. Mazilu, K. Dholakia, Nat. Photonics **2**, 675 (2008)
107. T.A. Planchon, L. Gao, D.E. Milkie, M.W. Davidson, J.A. Galbraith, C.G. Galbraith, E. Betzig, Nat. Methods **8**, 417 (2011)
108. T. Vettenburg, H.I.C. Dalgarno, J. Nylk, C. Coll-Llado, D.E.K. Ferrier, T. Cizmar, F.J. Gunn-Moore, K. Dholakia, Nat. Methods **11**, 541 (2014)
109. J. Arlt, T. Hitomi, K. Dholakia, Appl. Phys. B **71**, 549 (2000)
110. M. Mazilu, D.J. Stevenson, F. Gunn-Moore, K. Dholakia, Laser Photonics Rev. **4**, 529 (2009)
111. J.H. McLeod, J. Opt. Soc. Am. **44**, 592 (1954)
112. G. Roy, R. Tremblay, Opt. Commun. **34**, 1 (1980)
113. T. Grosjean, S.S. Saleh, M.A. Suarez, I.A. Ibrahim, V. Piquerey, D. Charraut, P. Sandoz, Appl. Opt. **46**, 8061 (2007)
114. J. Turunen, A. Vasara, A.T. Friberg, Appl. Opt. **27**, 3959 (1988)
115. A. Vasara, J. Turunen, A.T. Friberg, J. Opt. Soc. Am. A **6**, 1748 (1989)
116. J.A. Davis, J. Guertin, D.M. Cottrell, Appl. Opt. **32**, 6368 (1993)
117. N. Chattrapiban, E.A. Rogers, D. Cofield, W.T. Hill, R. Roy, Opt. Lett. **28**, 2183 (2003)
118. T. Cizmar, V. Kollarova, X. Tsampoula, F. Gunn-Moore, W. Sibbett, Z. Bouchal, K. Dholakia, Opt. Express **16**, 14024 (2008)
119. C. Maurer, A. Jesacher, S. Bernet, M. Ritsch-Marte, Laser Photonics Rev. **5**, 81 (2011)
120. V. Jarutis, R. Paskauskas, A. Stabinis, Opt. Commun. **184**, 105 (2000)
121. M.K. Bhuyan, F. Courvoisier, P.A. Lacourt, M. Jacquot, R. Salut, L. Furfaro, J.M. Dudley, Appl. Phys. Lett. **97**, 081102 (2010)
122. P. Polesana, A. Dubietis, M.A. Porras, E. Kucinskas, D. Faccio, A. Couairon, P. Di Trapani, Phys. Rev. E **73**, 056612 (2006)
123. D. Faccio, E. Rubino, A. Lotti, A. Couairon, A. Dubietis, G. Tamosauskas, D.G. Papazoglou, S. Tzortzakis, Phys. Rev. A **85**, 033829 (2012)
124. O. Brzobohaty, T. Cizmar, P. Zemanek, Opt. Express **16**, 12688 (2008)
125. J. Dudutis, P. Gecys, G. Raciukaitis, Opt. Express **24**, 28433 (2016)
126. F. Courvoisier, P.-A. Lacourt, M. Jacquot, M.K. Bhuyan, L. Furfaro, J.M. Dudley, Opt. Lett. **34**, 3163 (2009)
127. R. Sahin, Y. Morova, E. Simsek, S. Akturk, Appl. Phys. Lett. **102**, 193106 (2013)
128. Y. Matsuoka, Y. Kizuka, T. Inoue, Appl. Phys. A **84**, 423 (2006)
129. F. He, J. Yu, Y. Tan, W. Chu, C. Zhou, Y. Cheng, K. Sugioka, Sci. Rep. **7**, 40785 (2017)
130. A. Marcinkevicius, S. Juodkazis, S. Matsuo, V. Mizeikis, H. Misawa, Jpn. J. Appl. Phys. **40**, L1197 (2001)
131. M.K. Bhuyan, F. Courvoisier, P.-A. Lacourt, M. Jacquot, L. Furfaro, M.J. Withford, J.M. Dudley, Opt. Express **18**, 566 (2010)
132. M.K. Bhuyan, P.K. Velpula, J.P. Colombier, T. Olivier, N. Faure, R. Stoian, Appl. Phys. Lett. **104**, 021107 (2014)
133. P.K. Velpula, M.K. Bhuyan, F. Courvoisier, H. Zhang, J.-P. Colombier, R. Stoian, Laser Photonics Rev. **10**, 230 (2016)
134. M.K. Bhuyan, F. Courvoisier, H.S. Phing, O. Jedrkiewicz, S. Recchia, P. Di Trapani, J.M. Dudley, Eur. Phys. J. Spec. Top. **199**, 101 (2011)
135. L. Rapp, R. Meyer, R. Giust, L. Furfaro, M. Jacquot, P.A. Lacourt, J.M. Dudley, F. Courvoisier, Sci. Rep. **6**, 34286 (2016)

136. Y. Yu, L. Jiang, Q. Cao, B. Xia, Q. Wang, Y. Lu, Opt. Express **23**, 32728 (2015)
137. Q. Xie, X. Li, L. Jiang, B. Xia, W. Yan, W. Zhao, Y. Lu, Appl. Phys. A **122**, 136 (2016)
138. G. Wang, Y. Yu, L. Jiang, X. Li, Q. Xie, Y. Lu, Appl. Phys. Lett. **110**, 161907 (2017)
139. M.K. Bhuyan, O. Jedrkiewicz, V. Sabonis, M. Mikutis, S. Recchia, A. Aprea, M. Bollani, P. Di Trapani, Appl. Phys. A **120**, 443 (2015)
140. W.-J. Tsai, C.-J. Gu, C.-W. Cheng, J.-B. Horng, Opt. Eng. **53**, 051503 (2013)
141. L. Rapp, R. Meyer, L. Furfaro, C. Billet, R. Giust, F. Courvoisier, Opt. Express **25**, 9312 (2017)
142. P.K. Velpula, M.K. Bhuyan, C. Mauclair, J.-P. Colombier, R. Stoian, Opt. Eng. **53**, 076108 (2014)
143. M. Sakakura, M. Terazima, Y. Shimotsuma, K. Miura, K. Hirao, Opt. Express **15**, 5674 (2007)
144. M.K. Bhuyan, M. Somayaji, A. Mermillod-Blondin, F. Bourquard, J.P. Colombier, R. Stoian, Optica **4**, 951 (2017)
145. A. Vinçotte, L. Berge, Phys. Rev. Lett. **95**, 193901 (2005)
146. S. Shiffler, P. Polynkin, J. Moloney, Opt. Lett. **36**, 3834 (2011)
147. P. Polynkin, C. Ament, J.V. Moloney, Phys. Rev. Lett. **111**, 023901 (2013)
148. M.A. Porras, C. Ruiz-Jiménez, J. Opt. Soc. Am. B **31**, 2657 (2014)
149. V. Jukna, C. Milián, C. Xie, T. Itina, J. Dudley, F. Courvoisier, A. Couairon, Opt. Express **22**, 25410 (2014)
150. C.L. Arnold, S. Akturk, A. Mysyrowicz, V. Jukna, A. Couairon, T. Itina, R. Stoian, C. Xie, J.M. Dudley, F. Courvoisier, S. Bonanomi, O. Jedrkiewicz, P. Di Trapani, J. Phys. B **48**, 094006 (2015)
151. C. Xie, V. Jukna, C. Milián, R. Giust, I. Ouadghiri-Idrissi, T. Itina, J.M. Dudley, A. Couairon, F. Courvoisier, Sci. Rep. **5**, 8914 (2015)
152. K.T. Gahagan, G.A. Swartzlander, Opt. Lett. **21**, 827 (1996)
153. C. Hnatovsky, V.G. Shvedov, W. Krolikowski, A.V. Rode, Opt. Lett. **35**, 3417 (2010)
154. B. Wetzel, C. Xie, P.-A. Lacourt, J.M. Dudley, F. Courvoisier, Appl. Phys. Lett. **103**, 241111 (2013)
155. W. Cheng, P. Polynkin, J. Opt. Soc. Am. B **31**, C48 (2014)
156. R. Sahin, T. Ersoy, S. Akturk, Appl. Phys. A **118**, 125 (2015)
157. O. Jedrkiewicz, S. Bonanomi, M. Selva, P. Di Trapani, Appl. Phys. A **120**, 385 (2015)
158. T. Watanabe, M. Fujii, Y. Watanabe, N. Toyama, Y. Iketaki, Rev. Sci. Instrum. **75**, 5131 (2004)
159. V.V. Kotlyar, A.A. Almazov, S.N. Khonina, V.A. Soifer, J. Opt. Soc. Am. A **22**, 849 (2005)
160. J. Xin, K. Dai, L. Zhong, Q. Na, C. Gao, Opt. Lett. **39**, 1984 (2014)
161. M. Massari, G. Ruffato, M. Gintoli, F. Ricci, F. Romanato, Appl. Opt. **54**, 4077 (2105)
162. A. Volyar, V. Shvedov, T. Fadeyeva, A.S. Desyatnikov, D.N. Neshev, W. Krolikowski, Y.S. Kivshar, Opt. Express **14**, 3724 (2006)
163. W.C. Cheong, W.M. Lee, X.-C. Yuan, L.-S. Zhang, Appl. Phys. Lett. **85**, 5784 (2004)
164. R. Cao, Y. Yang, J. Wang, J. Bu, M. Wang, X.-C. Yuan, Appl. Phys. Lett. **99**, 261106 (2011)
165. L. Froehly, F. Courvoisier, A. Mathis, M. Jacquot, L. Furfaro, R. Giust, P.A. Lacourt, J.M. Dudley, Opt. Express **19**, 16455 (2011)
166. F. Courvoisier, A. Mathis, L. Froehly, R. Giust, L. Furfaro, P.A. Lacourt, M. Jacquot, J.M. Dudley, Opt. Lett. **37**, 1736 (2012)
167. E. Greenfield, M. Segev, W. Walasik, O. Raz, Phys. Rev. Lett. **106**, 213902 (2011)
168. M. Gecevicius, M. Beresna, R. Drevinskas, P.G. Kazansky, Opt. Lett. **39**, 6791 (2014)
169. A. Bahabad, M.M. Murnane, H.C. Kapteyn, Phys. Rev. A **84**, 033819 (2011)
170. A. Mathis, F. Courvoisier, L. Froehly, L. Furfaro, M. Jacquot, P.A. Lacourt, J.M. Dudley, Appl. Phys. Lett. **101**, 071110 (2012)
171. A. Mathis, L. Froehly, L. Furfaro, M. Jacquot, J.M. Dudley, F. Courvoisier, J. Eur. Opt. Soc. **8**, 13019 (2013)
172. A. Lotti, D. Faccio, A. Couairon, D.G. Papazoglou, P. Panagiotopoulos, D. Abdollahpour, S. Tzortzakis, Phys. Rev. A **84**, 021807 (2011)
173. D. Abdollahpour, S. Suntsov, D.G. Papazoglou, S. Tzortzakis, Phys. Rev. Lett. **105**, 253901 (2010)

174. R. Srinivasan, E. Sutcliffe, B. Braren, Appl. Phys. Lett. **51**, 1285 (1987)
175. S. Kuper, M. Stuke, Appl. Phys. B **44**, 199 (1987)
176. S. Kuper, M. Stuke, Appl. Phys. Lett. **54**, 4 (1989)